



A Wide View of the Galactic Globular Cluster NGC 2808: Red Giant and Horizontal Branch Star Spatial Distributions

Christian I. Johnson¹ , Annalisa Calamida¹ , Justin A. Kader² , Ivan Ferraro³, Catherine A. Pilachowski⁴ , Giuseppe Bono⁵ , Alessandra Mastrobuono-Battisti⁶ , Armin Rest¹ , Alfredo Zenteno⁷ , and Alice Zocchi⁸

¹ Space Telescope Science Institute, 3700 San Martin Drive, Baltimore, MD 21218, USA; chjohnson1@stsci.edu

² Department of Physics and Astronomy, 4129 Frederick Reines Hall, University of California, Irvine, CA 92697, USA

³ INAF—Osservatorio Astronomico di Roma Via Frascati 33 I-00040, Monte Porzio Catone, Italy

⁴ Department of Astronomy, Indiana University, SW 319, 727 East 3rd Street, Bloomington, IN 47405, USA

⁵ Department of Physics, Università di Roma Tor Vergata Via della Ricerca Scientifica 1 I-00133, Roma, Italy

⁶ GEPI, Observatoire de Paris, PSL Research University, CNRS Place Jules Janssen F-92190 Meudon, France

⁷ Cerro Tololo Inter-American Observatory NSF's National Optical-Infrared Astronomy Research Laboratory, Casilla 603 La Serena, Chile

⁸ University of Vienna Universitätsring 1 A-1010 Vienna, Austria

Received 2023 February 9; revised 2023 May 5; accepted 2023 May 8; published 2023 June 6

Abstract

Wide-field and deep DECam multiband photometry, combined with HST data for the core of the Galactic globular cluster NGC 2808, allowed us to study the distribution of various stellar subpopulations and stars in different evolutionary phases out to the cluster tidal radius. We used the $C_{ugi} = (u - g) - (g - i)$ index to identify three chemically distinct subpopulations along the red giant branch and compared their spatial distributions. The most light-element-enriched subpopulation (P3) is more centrally concentrated; however, it shows a more extended distribution in the external regions of the cluster compared to the primordial (P1) and intermediate (P2) composition populations. Furthermore, the P3 subpopulation centroid is off-center relative to those of the P1 and P2 groups. We also analyzed the spatial distribution of horizontal branch stars and found that the relative fraction of red horizontal branch stars increases for radial distances larger than ≈ 1.5 , while that of the blue and hotter stars decreases. These new observations, combined with literature spectroscopic measurements, suggest that the red horizontal branch stars are the progeny of all the stellar subpopulations in NGC 2808, i.e., primordial and light-element enhanced, while the blue stars are possibly the result of a combination of the “hot-flasher” and the “helium-enhanced” scenarios. A similar distribution of different red giant branch subpopulations and horizontal branch stars was also found for the most massive Galactic globular cluster, ω Cen, based on combined DECam and HST data, which suggests that the two may share a similar origin.

Unified Astronomy Thesaurus concepts: [Globular star clusters \(656\)](#)

Supporting material: machine-readable table

1. Introduction

NGC 2808 is one of the most massive ($M = 8.5 \times 10^5 M_{\odot}$; McLaughlin & van der Marel 2005) Galactic globular clusters (GGCs) and a very peculiar object. Hubble Space Telescope (HST) photometric investigations revealed that the cluster main sequence (MS) splits into a blue, an intermediate, and a red sequence. Furthermore, NGC 2808 shows an extended horizontal branch (HB) with distinct components: a red HB (RHB) and a blue tail divided into three groups (Sosin et al. 1997; Bedin et al. 2000). Therefore, it was suggested that NGC 2808 experienced multiple episodes of star formation, each with varying levels of helium enrichment and with the bluest MS representing the most enhanced population (Piotto et al. 2007; Milone et al. 2012, 2015b). The helium enrichment could also explain the observed HB morphology (D’Antona & Caloi 2004; D’Antona et al. 2005; Lee et al. 2005). Table 1 summarizes the basic properties of NGC 2808.

High-resolution spectroscopic measurements of ~ 140 red giant branch (RGB) stars in the cluster indicate that, while expected in the case of different star formation episodes, no

spread in iron content is present in NGC 2808 ($[\text{Fe}/\text{H}] = -1.192 \pm 0.004 \pm 0.034$; Carretta 2015). This already puzzling picture is complicated by the fact that the RGB evolutionary phase splits into five stellar populations with different light-element abundances (Carretta 2015).

Iannicola et al. (2009) combined HST and ground-based data covering a field of view (FOV) of $\sim 15' \times 15'$ centered on NGC 2808 to show that the relative fraction of cool (red) and hot (blue tail) HB stars is constant from the center to the outskirts of the cluster. This result supports the lack of radial differentiation among NGC 2808 stellar populations with possible distinct helium abundances. On the other hand, Simioni et al. (2016) showed that the intermediate and blue MS stars in NGC 2808, supposedly more helium enhanced, are more centrally concentrated compared to red MS stars, at least out to radial distances of $8'$ ($\sim 1/3$ of the tidal radius).

A proper-motion study based on HST data from Bellini et al. (2015) showed that the three MSs in NGC 2808 also have different kinematic behavior. At the outermost distance probed, $r \approx 1.5$, the velocity distribution of the intermediate and the blue MS stars is radially anisotropic, but it is isotropic for the stars belonging to the red MS. These findings might indicate the diffusion toward the cluster outskirts of the supposedly helium-enhanced populations, initially more concentrated. According to model predictions of the formation of GGCs

Table 1
Positional, Photometric, and Structural Parameters of the Galactic Globular Cluster NGC 2808

Parameter		References ^a
α (J2000)	138.0071	1
δ (J2000)	-64.8645	1
μ_α (2015)	0.994 ± 0.024	2
μ_δ (2015)	0.273 ± 0.024	2
M_V (mag) ^a	-9.4	3
r_c (arcmin) ^b	0.26	4
r_h (arcmin) ^c	0.86	5
r_t (arcmin) ^d	21.97	5
$\log(t_h)$ ^e	8.9	6
$E(B - V)$ ^f	0.19 ± 0.03	7
μ_0 (mag) ^g	15.05	3

Notes.

^a Total visual magnitude.

^b Core radius.

^c Half-mass radius.

^d Tidal radius.

^e Log of relaxation time.

^f Reddening.

^g True distance modulus.

References: (1) Gaia Collaboration et al. 2018; (2) Vasiliev & Baumgardt 2021; (3) Harris 2010; (4) Trager et al. 1995; (5) de Boer et al. 2019; (6) McLaughlin & van der Marel 2005; (7) Schlafly & Finkbeiner 2011.

with multiple stellar populations (MSPs), the second generation of stars should form in the inner regions (D’Ercole et al. 2008; Bastian et al. 2013): GGCs with a long relaxation time, such as NGC 2808 and ω Cen, should still show remnants of this initial spatial segregation.

A consensus on the origin of the different stellar subpopulations in NGC 2808 has not yet been reached. All previous investigations are based on data either for a few small fields across the center of the cluster (HST) or for an FOV covering about half the tidal radius (ground). There is now the need for a deep photometric study covering the entire cluster (tidal radius $r_t \sim 22'$; see Table 1; de Boer et al. 2019), with the precision necessary to enable the identification of the different RGB and HB groups.

In order to achieve this goal, we combined HST data for the core with deep *ugri* DECam photometry for NGC 2808. DECam is a wide-field imager covering a 3 deg^2 sky FOV (Figure 1). The high photometric quality and wide field covered by the combined DECam + HST photometric catalogs enable us to identify different RGB groups and to study their spatial distribution from the center to the cluster tidal radius. We also analyzed the distribution of red and blue HB stars and compared it to that of RGB, AGB, and MS stars.

Therefore, DECam photometry of NGC 2808 allowed us for the first time to investigate the spatial distribution of the different RGB subpopulations and different evolutionary phases from the core to the tidal radius and to discover their peculiarities.

2. Observations and Data Analysis

We collected a set of 207 *ugri* DECam images for NGC 2808 with NOAO proposals 2014A-0327, 2014B-0378, 2015B-0307, 2016A-0189, 2016A-0191, 2016B-0301, and 2017B-0279 (PI: Rest). In particular, we observed a couple of dozen deep ($t_{\text{exp}} = 600 \text{ s}$) *u*-band images in good observing

conditions in 2018 January, reaching an FWHM of $\approx 1''\text{--}1.2''$ on the images. The *u*-band photometry, which is sensitive to both effective temperature and metallicity, is critical for the color–color–magnitude method used here to separate cluster and field stars (Calamida et al. 2017, 2020). Moreover, the *u* filter is also fundamental to define the C_{ugr} index (Monelli et al. 2013) that we use to separate RGB stars with different light-element abundances.

A set of standard fields from SDSS Stripe 82 were also observed each night utilizing 15 s exposures for the *gri* bands and 30 s exposures for the *u* band. A total of 36 Stripe 82 images were obtained at varying air masses for each filter. These data were used to transform the instrumental magnitudes onto the DECam natural system (see Section 2.1).

A small number of additional, deep DECam exposures of NGC 2808 were also downloaded from the NOIRLab Astro Data Archive⁹ to supplement the data described above. These included 5 *gr*-band images from program 2013B-0615 (PI: Carballo-Bello) ranging between 200 and 300 s of integration; 4 *ugri*-band images from program 2013A-9999 (PI: Walker), each with 200 s of integration; and 12 *ugi*-band images from program 2012B-0001 (PI: Frieman) spanning 200–500 s of integration. Typical seeing was $\sim 1''$ for the 2013A-9999 data, $1.5''$ for the 2013B-0615 data, and $1.1''$ for the 2012B-0001 data.

We did not download any accompanying standard fields for the archival data, and instead we transferred the photometric calibration from our fields onto the archival data using stars in common between both sets. A log of all observations is presented in Table 2.

We also downloaded an HST catalog for NGC 2808 from the “Hubble Space Telescope UV Legacy Survey of Galactic Globular Clusters” (Piotto et al. 2015; Nardiello et al. 2018; GO13297; PI: Piotto). This catalog includes photometry collected with the Wide Field Camera 3 (WFC3) blue filters F275W, F336W, and F438W combined with ACS photometry in F606W and F814W by Sarajedini et al. (2007), and it covers the central $1'\text{--}2'$ of NGC 2808.¹⁰

The left panel of Figure 1 shows a density map of all DECam fields used in this project and indicates that the exposures extend well beyond the cluster tidal radius. However, the middle and right panels show that the DECam observations have a hole near the cluster core owing to the extreme crowding. Fortunately, this region is completely covered by the HST observations, which include both the ultraviolet (UV) bands necessary for identifying stars with different light-element abundances and the very high spatial resolution required to separate and photometer stars in the cluster core.

2.1. Photometry Pipeline, Calibration, and Catalog Preparation

The pipeline for generating intermediate catalogs with photometry, astrometry, errors, and associated quality flags closely followed the methods outlined in Johnson et al. (2020). To briefly summarize, the full focal plane DECam images, which were preprocessed with the DECam Community Pipeline (Valdes & Gruendl 2014), were separated into individual

⁹ The NOIRLab Astro Data Archive can be accessed at <https://astroarchive.noirlab.edu/>.

¹⁰ The HST data can be obtained from the Mikulski Archive for Space Telescopes (MAST) at the Space Telescope Science Institute by using DOI:10.17909/18ex-q697.

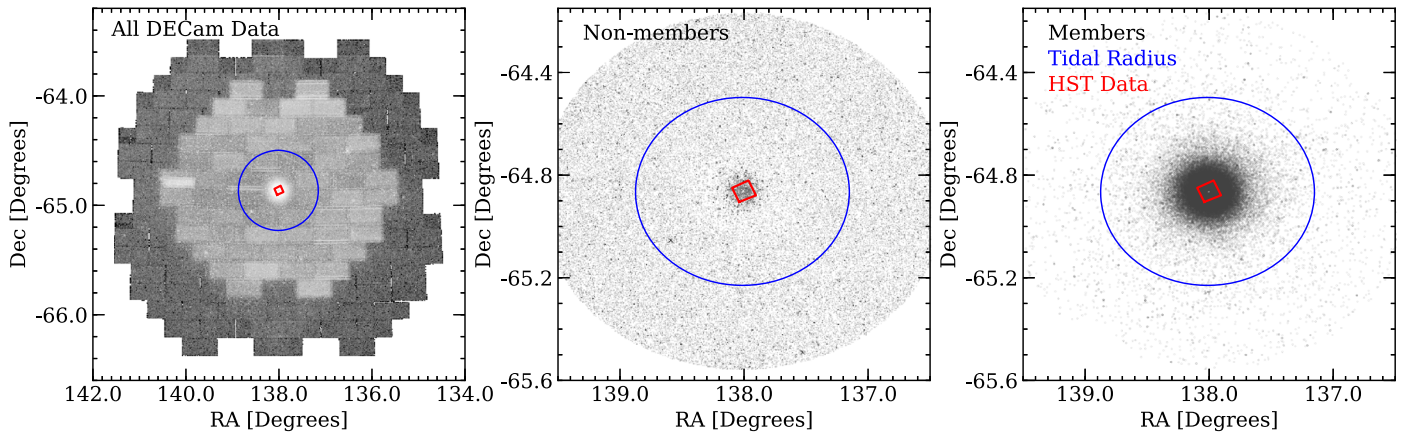


Figure 1. The left panel shows a source density map for all DECam data utilized in this project, with NGC 2808 at the center of the field. The middle and right panels show similar source density maps for the inner 40' region around NGC 2808 that was used to separate nonmember (middle) and member (right) stars. The blue circle in each panel highlights the tidal radius of 21'.97 adopted from de Boer et al. (2019), and the red box illustrates the location of archival HST observations that were used to fill a coverage gap in the very crowded cluster core ($r < 1.5$). Note that even though some stars observed near the cluster core with DECam were identified as nonmembers, most of these objects are inside the HST footprint for which we assumed 100% membership rates.

CCD files and then further partitioned based on filter, data set origin, and science/calibration status. All exposures were processed independently with DAOPHOTIV/ALLSTAR (Stetson 1987) on the science servers at the Space Telescope Science Institute, using an “embarrassingly parallel” code implementation. Both the science and calibration exposures were processed using quadratically varying point-spread functions (PSFs), along with a minimum of 25 and 10 PSF reference stars, respectively. Three “fit and subtract” loops were run on each exposure to identify additional faint stars and those in highly crowded fields.

A final processing step subtracted all photometered objects from each exposure except the bright and relatively isolated stars used for PSF fitting. DAOPHOT’s aperture photometry routine was run on these objects, in the subtracted images only, using a set of 12 sky apertures ranging from about 3 to 40 pixels in radius. The aperture photometry tables were then used to calculate growth curves via the DAOGROW algorithm from Stetson (1990), and the resulting aperture corrections were applied to the PSF photometry values in all images.

The r band was selected as the astrometric filter since it was observed every night and is in the middle of the wavelength range spanned by our observations. Following the methods outlined in Johnson et al. (2020, see their Section 3.3.1), we combined all of the r -band positions into a single table and generated a catalog of unique sources. Using a search threshold of $1''$, all objects detected in other bands were mapped onto the unique source table. The final list of unique sources totaled approximately 2×10^6 objects. A database was then created that linked all exposure and metadata (e.g., observation date, air mass, etc.) for each unique object so that the photometry could be merged.

Before merging the photometry, one exposure in each band was selected to serve as the zero-point reference frame. We only selected reference frames taken on the same nights as our SDSS Stripe 82 calibration fields. Median offset values were calculated between the reference frames and all other exposures of the same band using overlapping stars with magnitudes ranging from 14 to 18, after applying the necessary air-mass corrections. Mean (σ) image-to-image zero-point offsets for the $ugriz$ bands relative to the adopted reference frames were 0.008 (0.024), 0.005 (0.018), 0.007 (0.017), 0.002 (0.015), and 0.014

(0.017), respectively. With all of the data now on the same internal zero-point, the magnitude measurements and errors were combined for each filter via a weighted mean. The weights were determined by the inverse variance returned by DAOPHOT.

The absolute calibration for each filter was determined by comparing the SDSS Stripe 82 magnitudes measured here against a reference set converted onto the natural DECam system following the procedure described in Calamida et al. (2017). As a result, we only needed to calculate and apply a constant offset value for each band and could ignore color corrections. The accuracy of the calibration is $\approx 5\%$ for the bluer filters (ug) and $\approx 3\%$ for the redder filters (ri).

Although NGC 2808 is mildly affected by reddening along the line of sight (Bedin et al. 2000; $E(B - V) \approx 0.2$), the differential reddening is relatively small across our FOV. Figure 2 shows a reddening map for the FOV toward NGC 2808 based on the extinction values provided by Schlafly & Finkbeiner (2011). Cluster stars are overplotted as red circles in the plot. The figure shows that reddening is quite homogeneous for the central part of the cluster, while it may vary toward the outskirts. In particular, extinction seems slightly higher on the northeast quadrant of the FOV and lower in the southwest one. However, these regions are at and beyond the nominal tidal radius of NGC 2808 (22') and only include very few cluster stars ($\approx 1\%$). Moreover, the extinction for the entire 1.5×1.5 FOV is on average $E(B - V) \approx 0.18$ mag with a dispersion of $\sigma = 0.03$ mag. We also compared these reddening values with those from Gaia DR3 toward the FOV of NGC 2808 and obtained very similar results. Therefore, we did not apply any correction for differential reddening to our photometric catalog.

The final DECam photometric catalog includes 1,990,974 objects measured in the FOV. The largest number of stars was detected in the reddest filter (i ; $N = 984,942$), and the fewest stars were measured in the u filter ($N = 325,898$). The photometric catalog reaches a depth of $i \approx 21.5$ mag with a signal-to-noise ratio (S/N) of ≈ 50 . If we limit the photometry to observations including the u filter, the depth is $i \approx 21$ mag with S/N ≈ 70 .

Figure 3 shows the $i, u - i$, the $i, g - i$, and the $i, r - i$ color-magnitude diagrams (CMDs) for the entire sample of stars

Table 2
Log of NGC 2808 DECam Observations

File	Obs. Date	Proposal	PI	Filter	Exp. Time (s)	R.A. (deg)	Decl. (deg)	Seeing (arcsec)	Air Mass
c4d_160303_050811_ooi_i_v1	2016-03-03	2016A-0189	Rest	<i>i</i>	15	8:43:00.77	0:00:02.3	1.122	1.430
c4d_160303_050856_ooi_r_v1	2016-03-03	2016A-0189	Rest	<i>r</i>	15	8:43:00.50	0:00:05.4	1.281	1.430
c4d_160303_050941_ooi_g_v1	2016-03-03	2016A-0189	Rest	<i>g</i>	15	8:43:00.69	0:00:01.8	1.459	1.440
c4d_160303_051040_ooi_u_v1	2016-03-03	2016A-0189	Rest	<i>u</i>	30	8:43:00.83	0:00:06.4	1.604	1.440
c4d_160303_052102_ooi_r_v1	2016-03-03	2016A-0189	Rest	<i>r</i>	15	14:42:00.34	-0:04:27.7	1.267	1.800
c4d_160303_052144_ooi_i_v1	2016-03-03	2016A-0189	Rest	<i>i</i>	15	14:42:00.03	-0:04:28.3	1.105	1.800
c4d_160303_052227_ooi_g_v1	2016-03-03	2016A-0189	Rest	<i>g</i>	15	14:42:00.22	-0:04:24.2	1.404	1.790
c4d_160303_052326_ooi_u_v1	2016-03-03	2016A-0189	Rest	<i>u</i>	30	14:42:00.14	-0:04:24.9	1.469	1.780

Note. The full version of this table is provided in electronic form.

(This table is available in its entirety in machine-readable form.)

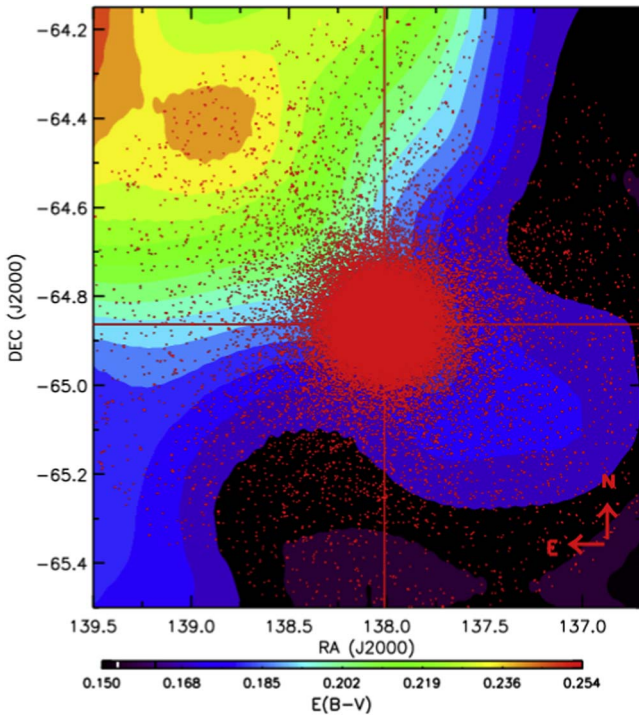


Figure 2. Reddening color density map as derived from Schlafly & Finkbeiner (2011) for stars toward the observed region across NGC 2808. Stars identified as cluster members from DECam photometric catalog are overplotted as red circles. The north and east directions are indicated with red arrows.

observed with DECam toward NGC 2808. The catalog was filtered by photometric accuracy, and $\approx 70\%$ of the best measured stars are plotted. Stars were also filtered by radial distance, to avoid the crowded regions of the cluster center, $r \geq 1.5$. The number of selected stars for each CMD is labeled in the figure.

Figure 3 clearly shows that NGC 2808 CMDs are strongly contaminated by field stars. However, some cluster evolutionary sequences are detectable, such as the HB for $16 \text{ mag} \lesssim i \lesssim 18.5 \text{ mag}$ and $g - i \lesssim 0.5 \text{ mag}$ and the RGB for $12.0 \text{ mag} \lesssim i \lesssim 16.0 \text{ mag}$ and $1.4 \text{ mag} \lesssim g - i \lesssim 2.5 \text{ mag}$. On the other hand, the lower part of the RGB, the MS turnoff (MSTO), and the lower MS are completely mixed with field stars. Gaia DR3 (Gaia Collaboration et al. 2022) proper-motion data for NGC 2808 are not complete in the more central cluster regions and have a limiting magnitude of $G = 21$, which is only 1 mag below the MSTO. Therefore, to separate the cluster and field

components, we used the same approach devised by Calamida et al. (2017, 2020). Briefly, we took advantage of the *u*-band observations to create a color-color-magnitude plane, *r* versus $g - i$ versus $u - r$, which better separates cluster and field stars owing to their different metallicities and gravities. We utilized an iterative procedure to select 74,262 candidate NGC 2808 member stars with at least one measurement in the *i* and *r* filters. The final cleaned catalog has 36,826 candidate cluster members with at least one measurement in all filters, *ugri*, and the CMDs are shown in Figure 4.

To verify the accuracy of our selection of cluster and field stars, we took advantage of Gaia DR3 data for the brighter portion of the photometric catalog. By matching using a radius of 0.5 , we found 12,702 stars in common with a DECam measurement in all filters and proper-motion measurement from Gaia. We then used the proper-motion plane to estimate how many stars might have been misidentified by our method as cluster stars. Gaia proper motion for NGC 2808 is $\mu_\alpha = 0.994 \pm 0.024 \text{ mas yr}^{-1}$ and $\mu_\delta = 0.273 \pm 0.024 \text{ mas yr}^{-1}$ (Vasiliev & Baumgardt 2021), and we selected as candidate cluster members stars with $-4 \text{ mas yr}^{-1} < \mu_\alpha < 5 \text{ mas yr}^{-1}$ and $-4 \text{ mas yr}^{-1} < \mu_\delta < 5 \text{ mas yr}^{-1}$. Of the 12,702 stars selected as NGC 2808 members with our color-color-magnitude method and in common with Gaia, 1139 are field stars according to proper motions, i.e., $\sim 9\%$. We repeated the same procedure for stars selected as field members from the color selection, and less than 1% are candidate cluster stars according to proper motions.

The clean sample of NGC 2808 stars is shown on the *i*, $u - i$, the *i*, $g - i$, and the *i*, $r - i$ CMDs of Figure 4. All the cluster sequences are clearly visible now, including the HB, divided into an RHB, clustering at $i \approx 15.8 \text{ mag}$, and a blue HB, extending down to $i \approx 20.5 \text{ mag}$. The MSTO is at $i \approx 19 \text{ mag}$, and the RGB extends from its base at $i \approx 18 \text{ mag}$ up to $\approx 12.5 \text{ mag}$. The RGB bump is also visible at $i \approx 15.5 \text{ mag}$.

In order to verify the accuracy of our photometric calibration, we compared the clean DECam CMD of NGC 2808 with models. We used two α -enhanced BASTI¹¹ isochrones for the same age, $t = 11 \text{ Gyr}$; two different metallicities, namely $Z = 0.002$ (blue solid line) and 0.003 (red); and two zero-age HB (ZAHB) tracks (Pietrinferni et al. 2021). These metallicity values, $-1.2 \leq [\text{Fe}/\text{H}] \leq -1.0$, bracket the iron abundance estimate from Carretta (2015). As a distance modulus we used $\mu_0 = 15.05 \text{ mag}$ and reddening

¹¹ <http://basti-iac.oa-abruzzo.inaf.it/index.html>

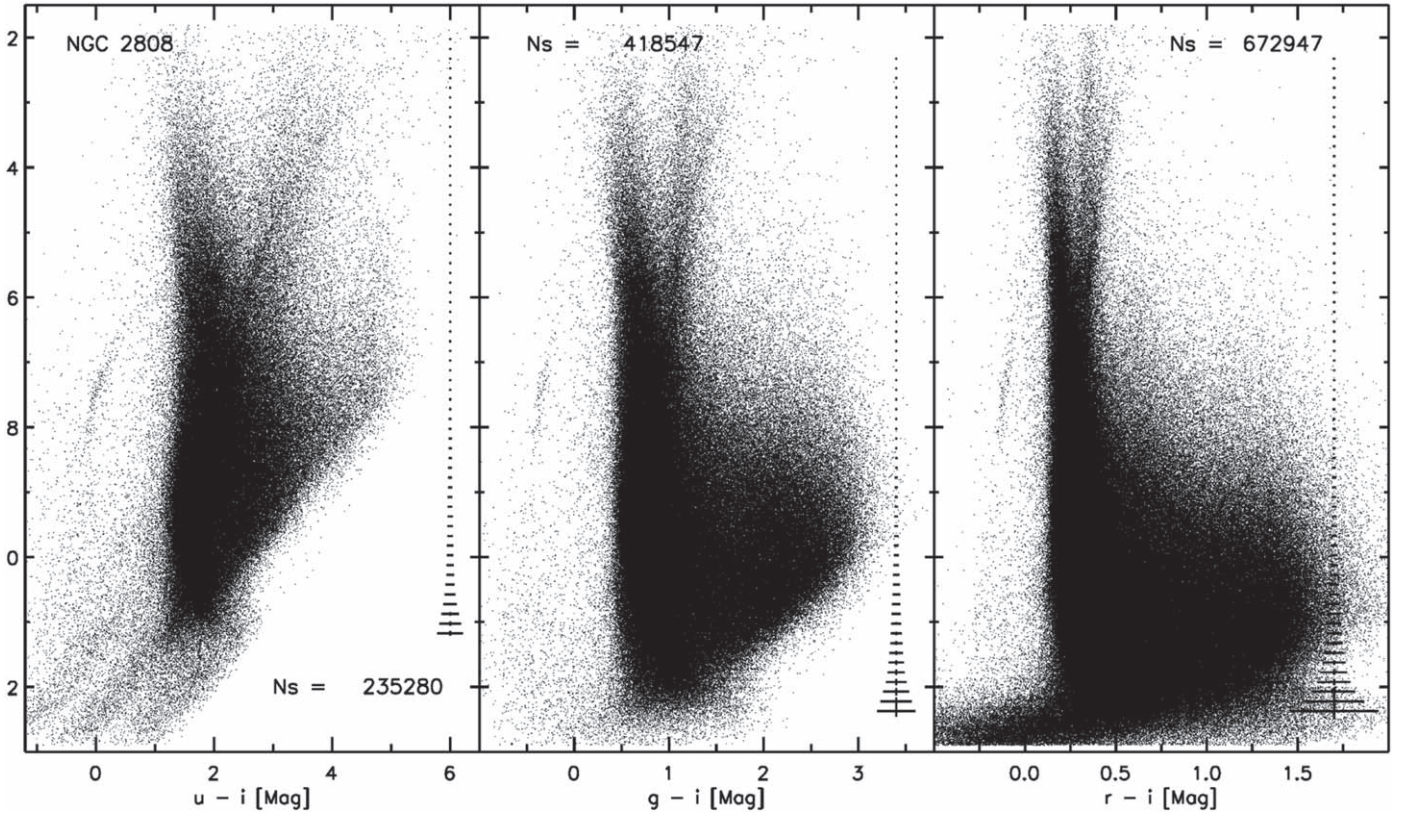


Figure 3. i vs. $u - i$, $g - i$, and $r - i$ CMDs are shown for the full DECam FOV. The cluster RGB, at $12.0 \text{ mag} \lesssim i \lesssim 16.0 \text{ mag}$ and $1.4 \text{ mag} \lesssim g - i \lesssim 2.5 \text{ mag}$, and blue HB, at $16.0 \text{ mag} \lesssim i \lesssim 18.5 \text{ mag}$ and $g - i \lesssim 0.5 \text{ mag}$, are clearly visible despite significant field star contamination. Error bars are shown.

$E(B - V) = 0.185$ (Schlafly & Finkbeiner 2011). This reddening value was converted into extinction in the DECam filters by using the Cardelli et al. (1989) reddening law and the available DECam filter throughputs.¹² We obtained $A_i = 0.63 \times A_V$ and $E(u - i) = 2.65 \times E(B - V)$, $E(g - i) = 1.70 \times E(B - V)$, and $E(r - i) = 0.65 \times E(B - V)$.

Figure 4 shows that the agreement between theory and observations is very good over the entire magnitude range in all three CMDs. The two isochrones bracket the NGC 2808 RGB and closely fit the MSTO, while the ZAHB models reproduce the HB from the red HB down to the blue tail.

3. Gaussian Mixture Models

We identify MSPs in NGC 2808 by fitting Gaussian mixture models (GMMs) to the distribution of the C_{ugi} color index of RGB stars. Color indices involving blue or UV filters, e.g., $C_{ugi, \text{DECam}} = (u - g) - (g - i)$ and the HST-equivalent $C_{ugi, \text{HST}} = (F336W - F438W) - (F438W - F814W)$, are effective diagnostics for separating MSPs because they are sensitive to light-element abundance variations. For example, star-to-star variations in Na abundance are correlated with a spread in the $C_{ugi, \text{DECam}}$ color since Na-poor stars are bluer in $u - g$ and redder in $g - i$, similar to $U - B$ and $B - I$ (Lardo et al. 2011; Monelli et al. 2013). Sample C_{ugi} CMDs using the DECam and HST observations are shown in Figure 5, which highlights that both data sets produce multiple distinct RGB sequences.

In order to construct the color distribution in the C_{ugi} index, it is necessary to first rectify the RGB since the color distribution we

are interested in should not include a contribution from the shape of the RGB. The color offset for each star is computed following the equation from Milone et al. (2017):

$$\Delta C_{ugi} = W_{C_{ugi}} \frac{X_{\text{fiducial}_R} - X}{X_{\text{fiducial}_R} - X_{\text{fiducial}_B}}, \quad (1)$$

which is the RGB-width-scaled offset from the red edge of the RGB, where $X = C_{ugi}$, and the “fiducial R” and “fiducial B” correspond to the red and blue fiducial curves, respectively. $W_{C_{ugi}}$ is the width of the RGB measured 1 mag brighter than the faintest RGB star. We determined the red and blue fiducial curves by evenly dividing the RGB into equal-width magnitude bins and in each bin computing the 4th and 96th percentiles in C_{ugi} color. The rectification procedure is summarized schematically in the left and middle panels of Figure 6.

Stars inside and outside of $r = 1.5$ were analyzed separately using HST and DECam photometry, respectively. Inner cluster stars were selected to have $-2.5 < C_{ugi, \text{HST}} < -1.6$ and $17.5 < F438W < 19$. The outer cluster stars were selected to have $-0.25 < C_{ugi, \text{DECam}} < 1.25$ and $14 < g < 18.6$. In both cases, we cut stars with photometric errors 3σ above the median photometric error and rejected stars with membership probabilities lower than 90%.

We estimated the number of sequences along the RGB using a Monte Carlo (MC) approach, where GMMs are repeatedly fit to the ΔC_{ugi} color distribution. At each iteration, we randomize the stellar magnitudes according to the photometric errors in each band. We also iterate over different magnitude bin widths ($0.05 < \Delta g$, $\Delta F438W < 0.25$) and the number of sigma clips to the RGB ($1 < N_\sigma < 20$). The MC simulation resulted in ~ 1000

¹² Information about the DECam filter throughputs can be found at <https://noirlab.edu/science/programs/ctio/filters/Dark-Energy-Camera>.

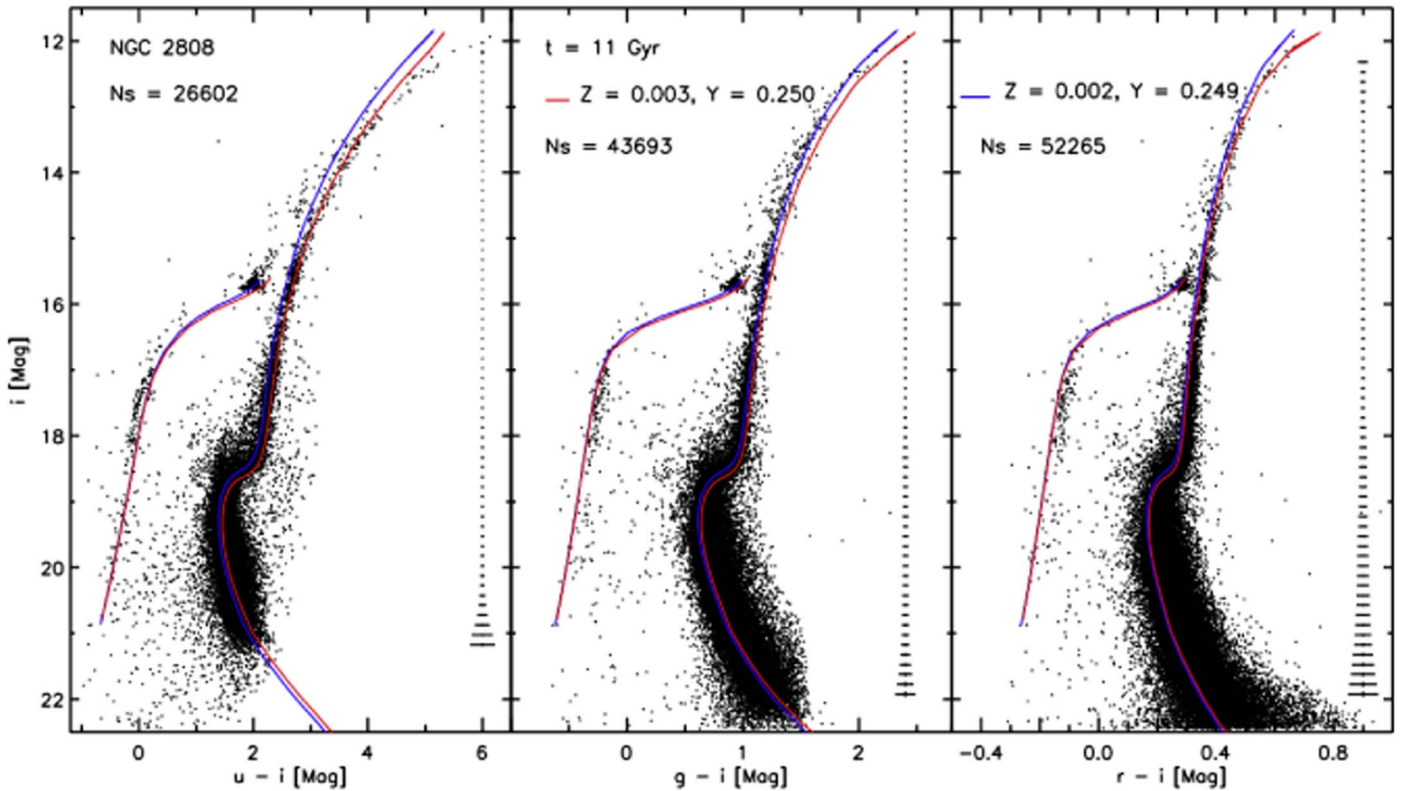


Figure 4. Same CMDs as those shown in Figure 3, except only candidate cluster members are shown. The CMDs are compared against BASTI isochrones and ZAHB models for different abundances and the same age as labeled in the figure. A distance modulus of $\mu_0 = 15.05$ and a reddening of $E(B - V) = 0.18$ mag were used. Error bars are shown. See text for more details.

realizations of the ΔC_{ugi} distribution. For each realization, the best of six GMMs (with $N_{\text{components}} = 1-6$) was determined using the Bayesian information criterion (BIC), which is similar to the χ^2 goodness-of-fit statistic but includes a term that penalizes for overfitting. The most frequently occurring value of $N_{\text{components}}$ was taken as our estimate for the number of sequences along the RGB. This procedure was done separately for stars inside $1/5$ (using HST photometry) and for stars outside $1/5$ (using DECam photometry). Figure 7 shows that for both data sets we find that the three-component GMMs best fit the data.

Population tagging of RGB stars was done using component membership probabilities assigned to the stars according to the best-fitting GMM. The probability that the i th star is a member of the j th mixture component (z_j) was estimated using the measured value of $\Delta C_{ugi,i}$ as input to the probability mass function for the component: $p(z_j = 1 | x_i = \Delta C_{ugi,i}) = P_j(\Delta C_{ugi,i})$. The right panels of Figure 6 show the $\Delta C_{ugi,HST}$ distribution for RGB stars inside (bottom) and outside (top) $r = 1/5$, with the best-fitting GMM overlaid. The HST and DECam photometric decompositions were made using magnitude bins with a width of 0.1 mag. For the HST data, we clipped stars in each bin with colors $> 3\sigma_{C_{ugi}}$, while for the DECam data we clipped stars with colors $> 5\sigma_{C_{ugi}}$.

4. Literature Comparison

4.1. Stellar Subpopulation Definitions

Although multiple chemically distinct groups have been found in NGC 2808, the nomenclature, separation of stars, and number of groups identified depend strongly on the data and analysis methods. For example, Piotto et al. (2007) identified

three MSs with different helium abundances via HST photometry and referred to these populations as “rMS,” “mMS,” and “bMS.” However, Latour et al. (2019) used a combination of HST photometry and MUSE/VLT (ESO) spectroscopy to identify four RGB populations (P1, P2, P3, and P4), while Hong et al. (2021) used CN, CH, and Ca H and K spectral indices to also find four RGB groups (G1, G2, G3, and G4). Furthermore, Carretta (2015) used various light-element abundance ratios to separate NGC 2808 stars into five groups (P1, P2, I1, I2, and E), and Milone et al. (2015a) used HST “chromosome maps” to identify five slightly different populations (A, B, C, D, and E).

More recently, Valle et al. (2022) used robust statistical methods to identify the different stellar populations in NGC 2808 by combining the high-resolution spectroscopy of Carretta (2015) and the low-resolution spectroscopy of Hong et al. (2021) and found only two groups along the cluster RGB, further complicating matters.

Table 1 of D’Antona et al. (2016) provides an approximate mapping between the Carretta (2015) and Milone et al. (2015a) groups, but the connection to similar nomenclature in other works is not straightforward.

Our GMM grouping algorithm identified three populations as the optimal number, regardless of whether the $C_{ugi,DECam}$ (ground-based) or $C_{ugi,HST}$ (space-based) data were used. We label these three populations as the P1, P2, and P3 groups, which correspond to stars having “primordial,” “intermediate,” and “extreme” chemical compositions. The P1, P2, and P3 populations constitute 31%, 38%, and 31% of our total RGB sample (3060 stars), respectively. We compared our $C_{ugi,DECam}$ designations against those of Carretta (2015),

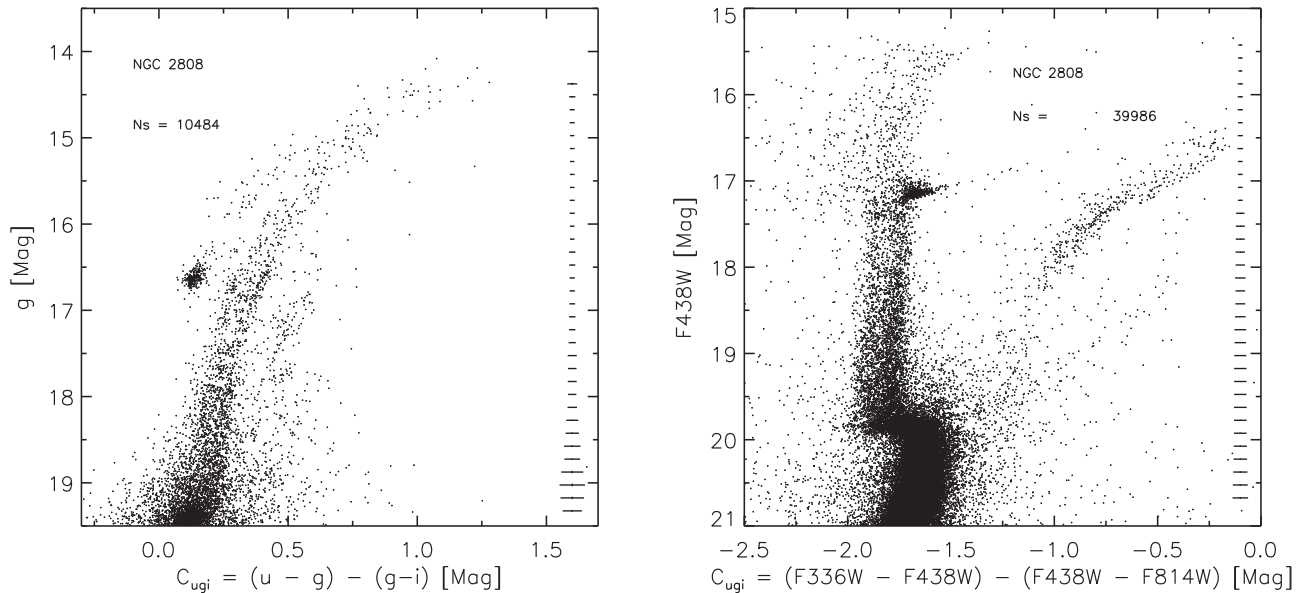


Figure 5. The $C_{ugi,DECam}$ CMD for NGC 2808 derived with DECam data is shown in the left panel, while a similar $C_{ugi,HST}$ CMD derived with HST data is shown in the right panel. Both data sets support the existence of at least two to three distinct RGB subpopulations. Note that the DECam data only include stars outside $1.5'$ from the cluster center, while the HST data trace stars inside $\sim 1.5'$.

Valle et al. (2022), and Hong et al. (2021) in Figures 8–9, and we correlated our $C_{ugi,HST}$ populations with those found in Latour et al. (2019) in Figure 10.

4.2. Stellar Subpopulation Matching

First, comparing our $C_{ugi,DECam}$ populations against those of Carretta (2015) in Figure 8, we found that the strongest correlation is between the “primordial” (P1) groups of both studies. For example, using the stars in common between the two studies, we found that 76% (16/21) of our P1 stars overlap with the P1_{C15} population, while the remaining 24% align with the adjacent P2_{C15} group; none align with the I1_{C15}, P2_{C15}, or E_{C15} groups. However, the correlations become more complicated for the enriched populations. Our P2 group, which is more chemically enhanced (lower [O/Fe], higher [Na/Fe]) than the P1 group, mildly overlaps with the P1_{C15}, P2_{C15}, I1_{C15}, and E_{C15} groups. Similarly, our P3 group overlaps with 25 stars in the Carretta (2015) sample, and these stars are distributed as 8% (2), 24% (6), 36% (9), 8% (2), and 24% (6) in the P1_{C15}, P2_{C15}, I1_{C15}, I2_{C15}, and E_{C15} populations, respectively. Therefore, we can align our P1 group with the P1_{C15} population with high confidence, and we consider our P2 + P3 groups to be a combination of the P2_{C15}, I1_{C15}, I2_{C15}, and E_{C15} populations from Carretta (2015). We note that the poor correlation between $C_{ugi,DECam}$ and the Carretta (2015) designations, particularly for more enriched stars, is due to the latter work targeting primarily cool, bright RGB stars. Figure 5 shows that the color separation in $C_{ugi,DECam}$ is narrower for stars significantly brighter than the RGB bump and also that AGB confusion increases for bright giants.

The right panel of Figure 8 shows that the correlations are somewhat stronger when adopting the two-population model from Valle et al. (2022). In this scenario, the Group 1 population from Valle et al. (2022) contains 100% of our overlapping P1 population, 75% of our P2 stars, and 44% of our P3 group, while their Group 2 population is almost entirely composed (83%; 15/18) of our most chemically enriched P3 stars. Combining the information from both panels of Figure 8

suggests that the $C_{ugi,DECam}$ color is highly sensitive for separating primordial and “second-generation” stars from each other, but that more nuanced separations with only these filters are difficult when analyzing only bright RGB stars. Therefore, a comparison between our $C_{ugi,DECam}$ population separation and that of Hong et al. (2021), which observed warmer stars, may provide more information about how the $C_{ugi,DECam}$ color separation correlates with populations identified via spectroscopy.

Figure 9 plots 82 stars in common between the present study and Hong et al. (2021) in the ΔCH versus ΔCN plane. We found a good correspondence between the $C_{ugi,DECam}$ photometry and spectroscopic populations, as well as a significantly reduced scatter compared to the results shown in Figure 8 for the brighter sample from Carretta (2015). We found that 83% (15/18) of the stars identified as belonging to the P1 group from $C_{ugi,DECam}$ photometry align with the G1 group from Hong et al. (2021), with the remaining 3 stars overlapping with the G2 group. Similarly, 94% (17/18) of our P3 stars align with the G3 and G4 populations from Hong et al. (2021). Our P2 population has the largest overlap (42%; 5/12 stars) with the G2 group, but it also has a handful of stars in the G1 (33%; 4/12), G3 (17%; 2/12), and G4 (8%; 1/12) groups. Therefore, we can associate our P1 and P2 populations with those of the G1 and G2 groups from Hong et al. (2021) and also find that their G3 and G4 groups combine to match our P3 population.

The top and middle panels of Figure 9 also validate our membership selection procedure for NGC 2808. In these panels, the black and gray circles indicate cluster members and field stars separated using our color–color–magnitude selection, respectively, while the purple and red symbols show stars from Hong et al. (2021) that are cluster members and field stars using the same criteria. The purple circles are located along NGC 2808’s RGB sequence, as expected, and the red circles overlap with field stars. In the proper-motion plane (middle panel), the purple circles overlap with the cluster stars, while the red circles are clearly offset with the field stars. When the handful of field stars are identified in the ΔCH – ΔCN plane

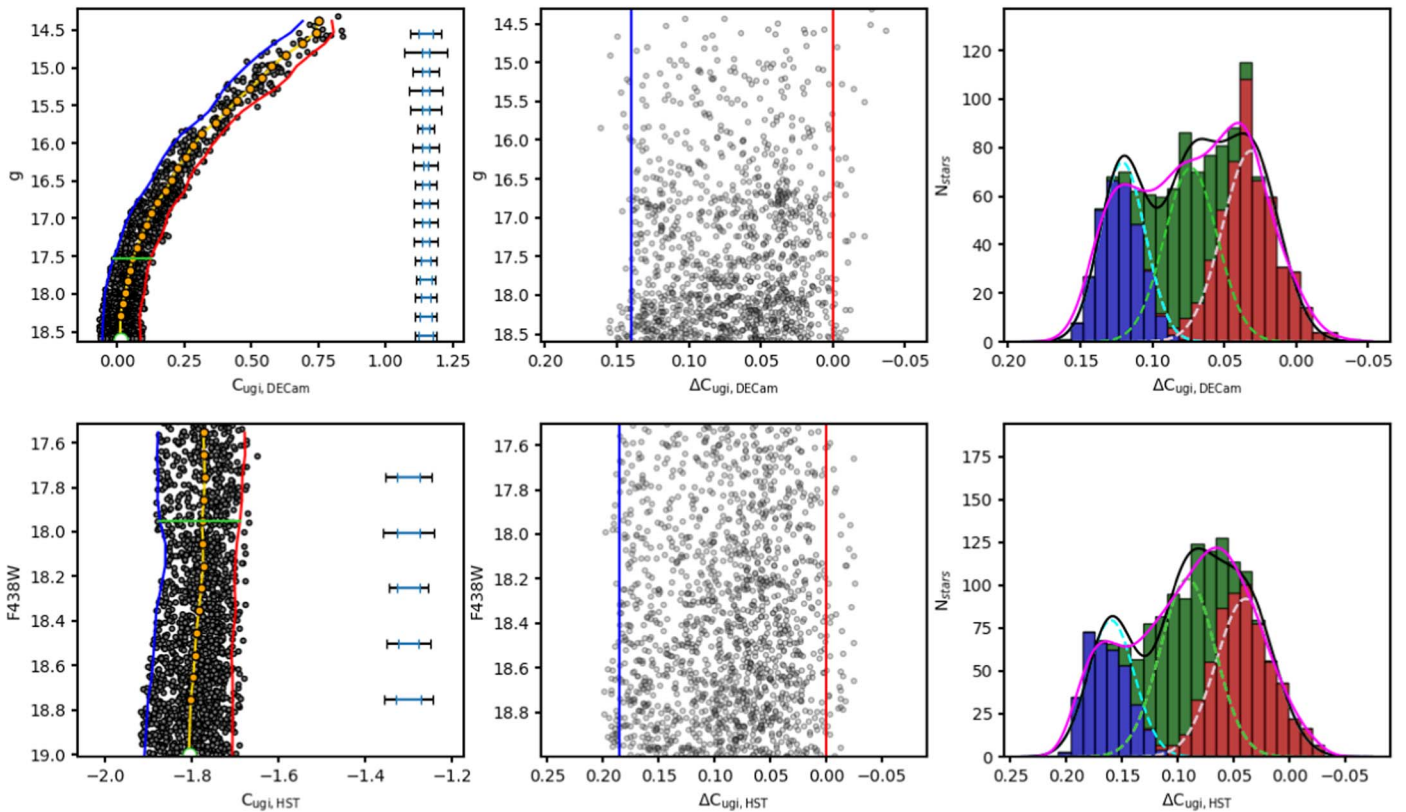


Figure 6. Demonstration of the technique used to divide NGC 2808 RGB stars into individual populations using photometry from DECam (top) and HST (bottom). The left panels show the g band (or equivalent F438W for HST) vs. C_{ugi} CMDs. The orange line is the median fiducial ridge line, and orange circles indicate the magnitude bin centers, which are separated by 0.1 mag. The 4th and 96th quantiles in C_{ugi} as a function of apparent magnitude are indicated with the blue and red curves, respectively. The magnitude at which we measure the RGB width is shown as a green line, which is 1 mag brighter than the faintest RGB star analyzed, which is indicated by the green open circle. The rms spread in C_{ugi} colors and the mean photometric error of stars along the RGB are shown as black and blue horizontal error bars to the left, respectively. The middle panels show the rectified RGBs, where the deviation from median RGB color is shown for each star as a function of magnitude. We collapse the rectified RGBs in the magnitude direction to reveal the individual sequences in ΔC_{ugi} , shown in the right panels. The best-fitting GMMs are overlaid on the ΔC_{ugi} histograms: individual components are colored blue, green, and red, and the sum is the black curve. The Gaussian kernel density estimation of the distribution is shown as a magenta curve.

(bottom panel), it becomes clear that these stars cause an artificial enhancement in the scatter of the nominal CH–CN anticorrelation. Two of the targets from Hong et al. (2021) are members according to their proper motions, but they are clearly offset from the cluster sequence. We suspect that these two stars were misidentified in the cross-match and have been removed from the analysis.

Finally, Figure 10 shows that we found a similar correlation between the $C_{ugi,HST}$ populations identified here and those found by Latour et al. (2019), which used the same data but included the F275W filter. Our P1 group is strongly correlated with the P1_{L19} population, and in general our P2 group aligns well with the P2_{L19} stars. However, we found some mild overlap between our P2 group and the P3_{L19} stars. Similarly, our P3 population matches a combination of the P3_{L19} and P4_{L19} groups. Therefore, we found a similar result when comparing with Latour et al. (2019) as with Hong et al. (2021), where our P1 group aligns with the P1_{L19} stars, our P2 group matches the P2_{L19} group, and our P3 population aligns with a combination of the P3_{L19} and P4_{L19} groups.

A summary of the mapping between our three HST and DECam populations and the various groups identified by Carretta (2015), Latour et al. (2019), Hong et al. (2021), and Valle et al. (2022) is provided in Table 3. In the next section, we will examine the radial profiles of the groups listed in this table and investigate differences in their distributions.

5. Radial Distributions

As noted previously, Carretta (2015) used high-resolution spectroscopy to divide a sample of 140 NGC 2808 RGB stars into five stellar populations (labeled P1_{C15}, P2_{C15}, I1_{C15}, I2_{C15}, and E_{C15} in Section 4.1). The data were further partitioned into three main groups, primordial (P), intermediate (I), and extreme (E), which aligned with the dominant populations identified in Carretta et al. (2009). When the radial distributions of the three main groups were analyzed, the author found that the combined I + E populations were more centrally concentrated than the P group, at least for distances between $\sim 1'$ and $5'$ from the cluster center, which is nominally in agreement with the cluster formation model described in D’Ercole et al. (2008). However, Carretta (2015) noted that their sample size was too small to draw any firm conclusions regarding radial distance variations between subpopulations.

Simioni et al. (2016) used WFC3 + ACS imaging on HST to photometrically separate the three dominant MS groups, which likely trace populations with different helium abundances (Piotto et al. 2007). The authors found that the blue (most extreme/He-rich) MS is the most centrally concentrated, while the middle MS stars are more concentrated than the red MS but less concentrated than the blue MS. Related to this work, Bellini et al. (2015) measured proper motions for a sample of NGC 2808 MS stars using ACS on HST and found no

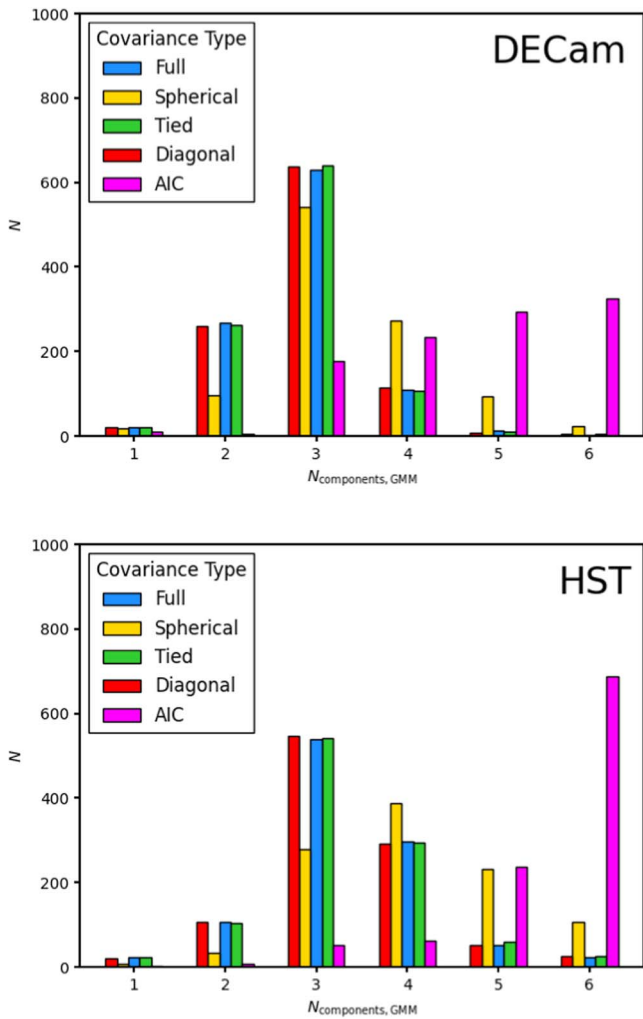


Figure 7. The various histograms show the optimal number of components derived from GMM realizations of the data using the BIC with all components sharing the same covariance matrix (“tied”; green), each component having a separate diagonal covariance matrix (“diagonal”; red), each component having its own covariance matrix (“full”; blue), and each component having a single variance value (“spherical”; yellow). The magenta histogram shows similar results but using the Akaike information criterion (AIC). Most methods found that a three-component fit was the optimal number.

differences in velocity dispersion for the various MS populations as a function of radial distance. However, their primordial MS groups (B and C) are nearly isotropic, while the more enriched populations (D and E) are radially anisotropic; these most enriched stars also have smaller tangential velocity dispersions.

Bellini et al. (2015) showed that the strongest deviations from isotropy are in the outer parts of the cluster (for distances larger than $\approx 2r_h$). Furthermore, the authors provide a simulation that demonstrates how enriched stars that are initially more centrally concentrated disperse with time on preferentially radial orbits (see also Mastrobuono-Battisti & Perets 2013; Hénault-Brunet et al. 2015; Mastrobuono-Battisti & Perets 2016). As a result, many enriched stars that are now in the outer parts of the cluster may have initially formed in the core and dispersed outward, and thus a cluster’s various subpopulations may have different kinematic and radial density profiles. As long as a cluster’s dynamical evolution is not too advanced, kinematic and radial density differences between primordial and enriched stars may still be observable after a

Hubble time (e.g., Vesperini et al. 2013; Mastrobuono-Battisti & Perets 2016; Vesperini et al. 2021; Tiongco et al. 2022).

NGC 2808 has a multimodal HB, as shown by different ground- and space-based photometric investigations, with an RHB and a blue tail divided into three groups (Sosin et al. 1997; Bedin et al. 2000; Castellani et al. 2006; Iannicola et al. 2009). The origin of this multimodal HB has been attributed to different “second” parameters, such as age, mass loss along the RGB due to rotation or binarity, the “hot-flasher” scenario, and/or helium enrichment (D’Cruz et al. 1996; Catelan et al. 1998; Sweigart & Catelan 1998; Brown et al. 2001; Moehler et al. 2004; D’Antona et al. 2005; Lee et al. 2005; Castellani et al. 2006).

Walker (1999) and Bedin et al. (2000) used ground-based photometry of NGC 2808 to study the radial distribution of the different groups of HB stars and found no gradient across most ($4' - 6'$) of the cluster body (note that NGC 2808 tidal radius is $r_t \approx 22'$; see Table 1). However, a subsequent investigation based on UV HST photometry by Castellani et al. (2006) found a radial trend in the ratio of HB stars to the number of RGB stars brighter than the ZAHB luminosity level, the so-called R parameter. In particular, this ratio increases from the expected value of $R \approx 1.4$ (Zoccali et al. 2000; Cassisi et al. 2003) in the cluster center to ≈ 1.7 at $2'$ distance. They propose different hypotheses for the extended distribution of the HB stars, such as high-intensity mass loss along the RGB-producing “blue hook” HB stars through the “hot-flasher” scenario and/or a dynamical origin. Note that their HST data sets do not cover radial distances larger than $\approx 2'$.

Sohn et al. (1998) found a color gradient when analyzing ground-based photometric observations of NGC 2808, with the central regions ($r < 70''$) being redder than the outskirts. As an explanation, they proposed an excess of RGB stars in the cluster core. On the other hand, Sandquist & Martel (2007) showed that NGC 2808 has a paucity of bright RGB stars compared to model predictions, possibly confirming a larger mass loss during this evolutionary phase, with a delayed or missed helium flash.

Furthermore, Iannicola et al. (2009) confirmed a flat radial distribution of HB stars in NGC 2808, as previously found by Walker (1999) and Bedin et al. (2000), based on HST and ground-based photometry of the cluster. They also found that the R parameter increases toward the outskirts of the cluster, and they explain this with a decrease of bright RGBs in these regions. However, their result might be hampered by the contamination of field stars that could artificially increase the number of RHB stars.

All the aforementioned results on the spatial distribution of the different RGB subpopulations and multiple HBs in NGC 2808 are based on heterogeneous photometric catalogs limited to radial distances less than $\approx 4'$. Our deep and precise combined DECcam + HST photometric catalog will now allow us to perform a thorough analysis of the radial distribution of the three different stellar subpopulations we identified on the RGB and the multiple HBs across the entire extent of NGC 2808.

5.1. RGB Stars

The RGB radial distribution investigation executed in the present work includes >3000 high membership probability stars brighter than $g_{\text{DECcam}} = 18.5$ and $F438W_{\text{HST}} = 19.0$ mag ranging from near the cluster core to about the tidal radius.

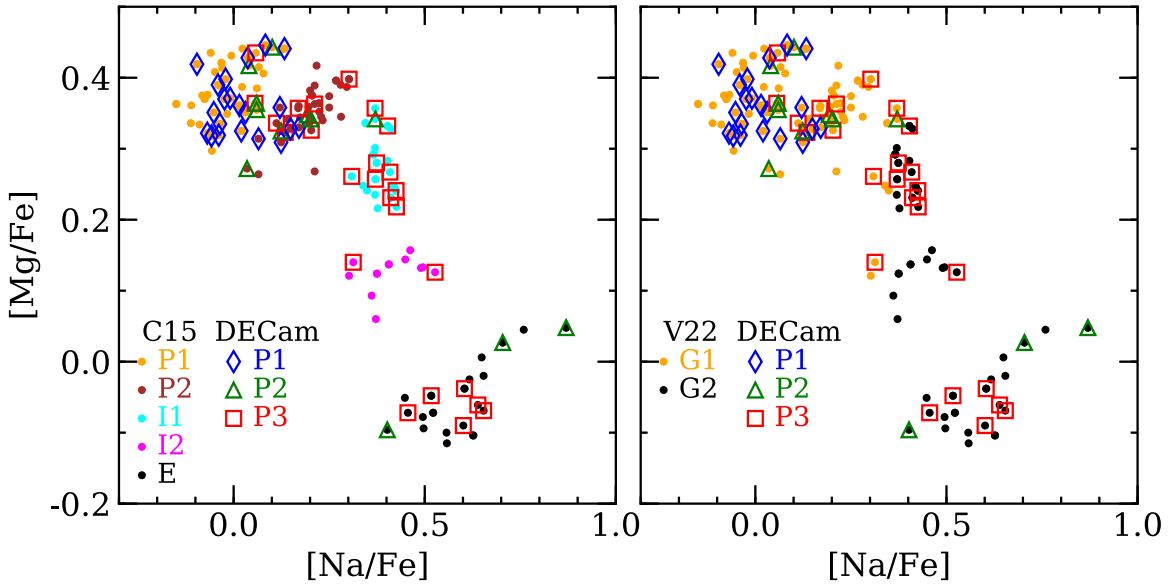


Figure 8. The left panel shows the $[\text{Mg}/\text{Fe}]$ vs. $[\text{Na}/\text{Fe}]$ abundances from Carretta (2015) for NGC 2808 RGB stars. Each of the five populations identified by Carretta (2015) is shown as a different-colored filled circle. Cross-matched populations from our DECcam $C_{\text{ugi,DECcam}}$ decomposition are shown as different-colored large open symbols. In general, we find that both studies cleanly separate primordial (P1) stars from those that formed from gas processed at higher temperatures. The $C_{\text{ugi,DECcam}}$ index generally finds that P3 stars have higher $[\text{Na}/\text{Fe}]$ and lower $[\text{Mg}/\text{Fe}]$ than those in the P2 group, but both populations are somewhat mixed. The mixing of P2 and P3 stars is likely because the Carretta (2015) sample mostly consists of bright RGB stars, where the $C_{\text{ugi,DECcam}}$ separation is small. Similarly, the right panel shows the same data but with the Carretta (2015) sample separated into only two groups, based on the reanalysis by Valle et al. (2022).

Since Section 4.2 confirmed that the C_{ugi} pseudocolor is strongly correlated with RGB light-element composition, we can use this information to analyze the different radial density profiles of the P1, P2, and P3 populations.

Figure 11 summarizes the different radial distribution profiles for the three main subpopulations identified from the GMM procedure outlined in Section 3, with the HST and DECcam data analyzed separately. The left panels of Figure 11 show the number of stars for a given subpopulation within each radial bin but normalized to the bin of maximum height for each group. Similarly, the right panels show the cumulative distributions of the same data. These panels highlight a few interesting trends. First, the P3 stars (most Na-rich according to the comparison with spectroscopy) appear to be the most centrally concentrated inside ≈ 0.7 ($\approx 0.88r_h$); however, the P3 trend flattens out substantially at larger radii. For distances ranging from $\approx 1'$ to $5'$ from the cluster core, the P2 (intermediate enrichment) stars are more centrally concentrated than both the P3 and P1 (primordial) populations. The flatter P3 radial density distribution extends out to at least 10 half-mass radii, but the number of stars in each subpopulation becomes too small to differentiate trends between the three groups at larger distances.

Figure 12 compares normalized isodensity contours for the P1, P2, and P3 subpopulations over the full range of radial distances considered here. The panels again highlight that the P2 subpopulation is more centrally concentrated than the P1 and (especially) P3 groups when extending to distances far from the cluster center. Similarly, Figure 12 shows that the 50% contour level of the P3 group covers an area that is nearly $2\times$ larger than either the P1 or P2 subpopulations. The bottom right panel of Figure 12 also shows mild evidence that the P3 population may have a slightly different position angle that is rotated northward compared to the P1 and P2 groups. However, one of the most intriguing results from Figure 12 is that the P3 subpopulation centroid appears offset relative to the nominal

cluster center and also relative to the P1 and P2 centroids. An MC simulation with 10,000 resamplings of the population designations, based on the probabilities assigned in Section 4.2 to each star, indicates that the P3 group centroid is offset from the P1 and P2 population centers by $\approx 6''.0-6''.5$ ($0.14r_h$), with most of the shift coming from the R.A. coordinate.

5.2. HB Stars

We used here our DECcam + HST deep and precise photometry, which covers more than the entire tidal extent of NGC 2808, to investigate the radial distribution of the HB stars. As a first step, HST photometry in the F438W, F606W, and F814W filters was converted into the DECcam g , r , and i filters. A sample of bright and well-measured stars in common between the two data sets was selected, and the following color transformations were derived:

$$g = \text{F438W} - 0.05 - 0.27 \times (\text{F438W} - \text{F814W}) \quad (2)$$

$$r = \text{F606W} + 0.11 - 0.29 \times (\text{F606W} - \text{F814W}) \quad (3)$$

$$i = \text{F814W} + 0.27 + 0.14 \times (\text{F606W} - \text{F814W}). \quad (4)$$

Figure 13 shows the r , $g-i$ CMDs based on HST photometry for radial distances $r \leq 1.5$ (left panel) and DECcam for $r > 1.5$ (right). NGC 2808 HB stars were divided into four groups, namely RHB, EBT1, EBT2, and EBT3, following the prescriptions of Bedin et al. (2000), Castellani et al. (2006), and Iannicola et al. (2009), and stars were counted; errors were calculated as the square root of the number counts. Table 4 lists the number counts of the HB stars identified in each group and data set with their uncertainties.

Figure 14 shows the r -band luminosity function for NGC 2808 HB based on HST (top panel) and DECcam photometry (bottom). Note that the completeness of both catalogs is quite similar at these luminosity levels.

It is interesting to note that the RHB fraction increases in the outskirts of NGC 2808, i.e., for distances larger than ≈ 1.5 , i.e.,

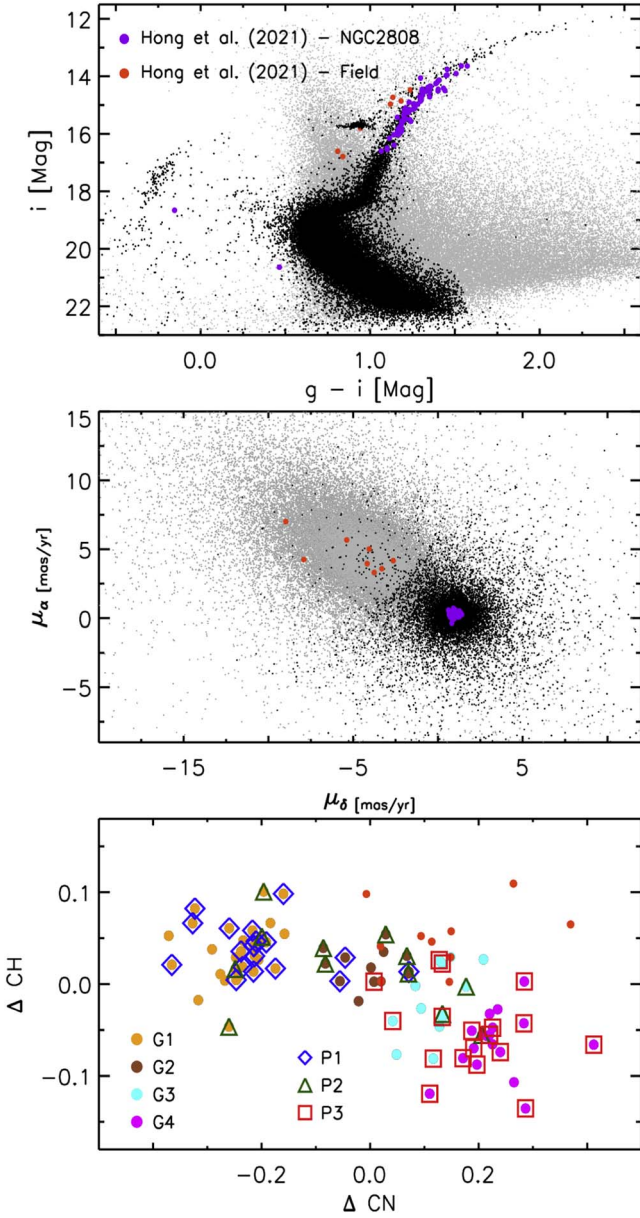


Figure 9. Top: DECAM i , $g - i$ CMD for NGC 2808 candidate member stars (black circles) and for candidate field stars (gray) according to the color–color–magnitude selection. The 82 stars in common with the spectroscopic study of Hong et al. (2021) are overlotted as purple (NGC 2808 members) and orange circles (field). Two of the candidate cluster members are not on the RGB (see text for more details). Middle: same stars plotted on the Gaia proper-motion plane. Bottom: the 82 stars with spectroscopy are plotted on the ΔCN vs. ΔCH plane: the four groups identified by Hong et al. are marked with different colors and labeled as G1, G2, G3, and G4. The stars for which we derive the C_{ugi} index and separate into three groups are marked with different symbols and labeled as P1, P2, and P3. The 10 stars from Hong et al. that are classified as field members by our color–color–magnitude selection and Gaia proper motions are marked as orange filled circles.

$\approx 2r_h$; on the other hand, the number of EBT1 and EBT3 stars decreases, while the number of EBT2 stars is approximately constant. However, the DECAM sample of RHB stars might be more affected by residual contamination of field stars compared to the bluer HB stars. In order to investigate this issue, we matched DECAM HBs with the Gaia DR3 catalog and found 460 (out of 490) stars in common, and 441 of these have a proper-motion measurement. Note that only 6 out of 29 EBT3 stars were found in Gaia, due to their faintness. On the other

hand, all except two stars of the RHB group were found; therefore, we used the proper motion of NGC 2808 calculated by the Gaia Collaboration et al. (2018; see Table 1) and selected as candidate cluster members RHB stars with $-4 \text{ mas yr}^{-1} < \mu_\alpha < 5 \text{ mas yr}^{-1}$ and $-4 \text{ mas yr}^{-1} < \mu_\delta < 5 \text{ mas yr}^{-1}$. Of 266 RHBs, 261 are cluster members, resulting in a $\approx 2\%$ residual contamination of field stars. In the case of the EBT1 star group, all of the 136 stars with Gaia proper-motion measurement are cluster members, with a $\approx 0\%$ residual contamination from the field. We could not perform the same calculation for the EBT2 and EBT3 groups, since these are highly incomplete in the Gaia catalog. However, a large residual contamination by field stars is not expected at these very blue colors, $g - i \lesssim 0$ mag (see the CMDs in Figure 3).

We then selected RGB stars brighter than the RHB luminosity level in both r , $g - i$ CMDs, where the RHB is approximately flat for colors $g - i \gtrsim 0.5$ mag, and calculated the R parameter, i.e., the ratio of the number of HB stars over the number of RGB stars brighter than the RHB, as a function of distance from the cluster center, r . Stars were selected in concentric annuli of different thicknesses, to allow the number of objects per annulus to be always larger than ≈ 20 . We assumed a Poisson error on the star number counts and calculated the uncertainty on the ratio as

$$\begin{aligned} \text{Err}(R) &= R \cdot \sqrt{\left(\frac{dX}{X}\right)^2 + \left(\frac{dY}{Y}\right)^2} \\ &= R \cdot \sqrt{\frac{1}{X} + \frac{1}{Y}} = R \cdot \sqrt{\frac{X+Y}{X \cdot Y}}, \end{aligned} \quad (5)$$

where $R = X/Y$ and X and Y are the number of HB and RGB stars in this case, and $\text{Err}(X) = \sqrt{X}$ and the same for Y .

The top panel of Figure 15 shows the R parameter, $N(\text{HB}/\text{RGB})$, as a function of radial distance r in arcminutes, based on HST photometry for $r \leq 1.5'$ and on DECAM photometry for the external regions. In the case of the HST data set we only selected stars for $r \geq 0.3'$, since the catalog is not complete closer to the cluster center owing to crowding effects. Regarding DECAM photometry, we calculated the R parameter up to a radial distance of $6'$, since the number of stars greatly decreases for larger distances, with less than 40 RGB and 40 HB stars in the last two annuli, and the uncertainties on the ratios increase.

The R parameter is ≈ 1.5 (dashed line in the figure) inside the half-mass radius, r_h (dotted line), while it is systematically lower in the external regions, with a mean value of 1.16 ± 0.27 , or 1.05 ± 0.25 , excluding the last two annuli. For radial distances larger than $\approx 5'$, R slightly increases again, but the uncertainty is a factor of two larger in these more external regions of NGC 2808.

The decrease of the R parameter with radial distance could be due to an increased contamination of the RGB sample by field stars toward the external regions of NGC 2808. To investigate this issue, we matched the RGB stars with the Gaia DR3 catalog and found 434 (out of 444) stars in common and with a proper-motion measurement; of these, 419 are cluster members ($\approx 97\%$). About half of the contaminant stars (7/15) are located at radial distances larger than $9'$, so outside the range of distances of our analysis (Figure 15). Therefore, we can safely claim that contamination by field stars of the RGB sample does not affect the decrease of the R parameter with radial distance.

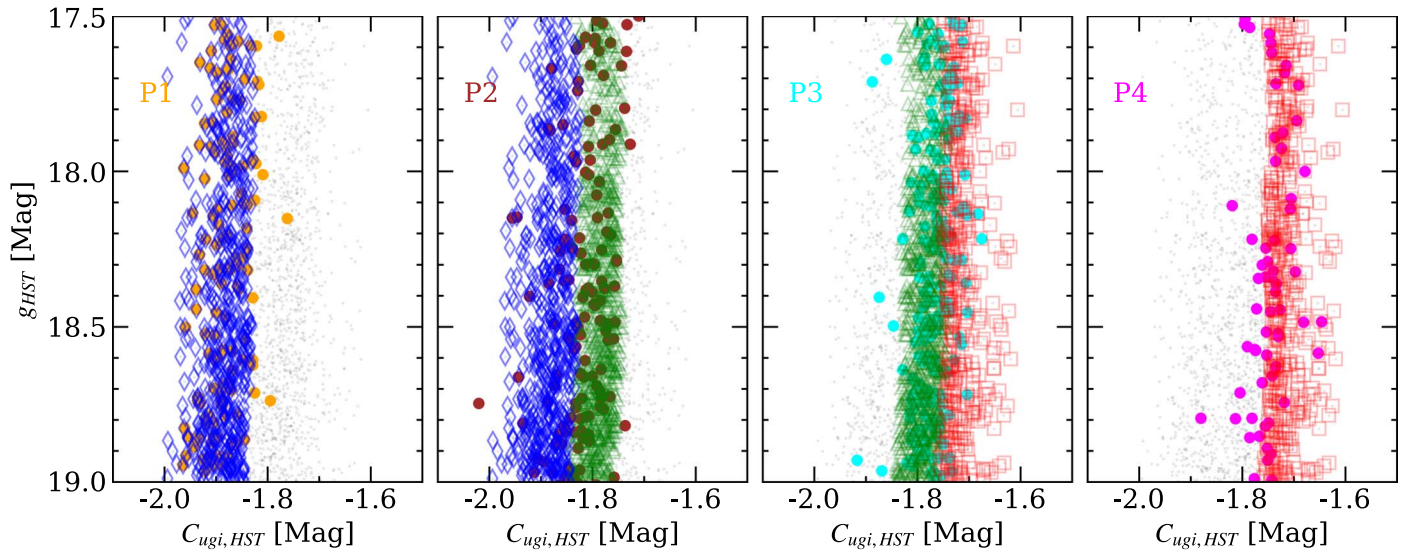


Figure 10. $C_{ugi,HST}$ CMDs are shown with the four populations from Latour et al. (2019), which were identified using chromosome maps that include the F275W filter, indicated as large orange, brown, cyan, and magenta circles. The open symbols represent the HST-equivalent P1 (blue), P2 (green), and P3 (red) populations identified in Figure 8 for our DECam data and use the same color/symbol shape scheme. The small light-gray circles illustrate the full width of the $C_{ugi,HST}$ color range. The comparison shows that the P1 group from Latour et al. (2019) is strongly mapped to our P1 group, their P2 group is relatively well aligned with our P2 group, and their P3/P4 groups are a mixture of our P2 and P3 groups. This figure highlights the strong correlation between the $C_{ugi,HST}$ index and similar indices that use F275W.

Table 3

Population Correspondence

Reference	P1 _{ours}	P2 _{ours}	P3 _{ours}
Carretta (2015)	P1 _{C15}	(P2 + I1 + I2 + E) _{C15}	(P2 + I1 + I2 + E) _{C15}
Valle et al. (2022)	Group 1 + Group 2	Group 1 + Group 2	Group 2
Hong et al. (2021)	G1	G2	G3 + G4
Latour et al. (2019)	P1 _{L19}	P2 _{L19}	(P3 + P4) _{L19}

In order to further assess the cause for the decrease of the R parameter, we also calculated the ratio of the number of HB and RGB stars over the number of MS stars in the same cluster region. We only selected MS stars in a narrow magnitude range around NGC 2808 MSTO point, $19.2 \text{ mag} \leq r \leq 19.5 \text{ mag}$, to avoid the number counts being dependent on the mass function of the cluster (see Figure 13).

The ratio of the number of RGB and HB stars over the number of MS stars as a function of radial distance is shown in the middle and bottom panels of Figure 15, respectively: $N(\text{RGB}/\text{MS})$ seems to increase at distances $r \approx 1'.7$ and then to decrease, attaining a constant value of ≈ 0.12 (dashed line in Figure 15) throughout the extent of the cluster. On the other hand, the $N(\text{HB}/\text{MS})$ is about constant, ≈ 0.17 (dashed line), until a radial distance of $\approx 2'.70$, and then it slightly decreases to ≈ 0.12 at larger distances.

These ratios suggest that the culprit for the decrease of the R parameter at radial distances larger than $1'.5$ are the HB stars, in the sense that their total number decreases in the outskirts of NGC 2808.

In order to better understand the trend of the radial distributions of the stars belonging to different evolutionary phases, we also calculated the ratio of the number of AGB stars over the number of RGB stars (brighter than the RHB): $N(\text{AGB})/N(\text{RHB}) = 0.13 \pm 0.01$ for radial distances $< 1'.5$, and

0.16 ± 0.02 at larger distances. The number of AGB stars is also listed in Table 4. To check for possible field star contamination of the AGB sample in the external regions of NGC 2808, we matched DECam AGB candidates with Gaia DR3 and found 66 stars in common and with proper-motion measurements. We applied the same selection criteria as before and found that 88% of these stars are cluster members. By removing the number of possible field contaminants from both the AGB and RGB samples, the ratio of the number of AGB stars over the number of RGB stars in the external regions of the cluster is 0.15 ± 0.02 , still slightly larger than the value closer to the cluster center. These ratios would suggest a slight increase of the number of AGB stars in the outer regions of NGC 2808. We then calculated the ratio of the number of AGB stars compared to the number of RHB stars in both regions and obtained $N(\text{AGB})/N(\text{RHB}) = 0.21 \pm 0.02$ and 0.26 ± 0.03 , respectively. When taking into account the possible contamination by field stars of both samples, the ratio of AGB over RHB stars is 0.23 ± 0.02 in the external regions of the cluster. These data suggest a similar distribution of AGB and RHB stars, which is expected since most RHBs should evolve along the AGB branch.

We were not able, unfortunately, to compare the star counts of the AGB-manqué stars with those of their progenitors, the blue HB stars, since we do not have precise and deep UV photometry for a wide FOV across NGC 2808 that would allow us to identify the AGB-manqué stars (the bluest DECam filter is the u band, with a central wavelength of $\approx 3560 \text{ \AA}$).

Figure 14 shows the r -band luminosity function of the full HB of NGC 2808 as a function of distance from the cluster center; from this plot it is clear that the number of RHB stars increases in the more external regions of NGC 2808 while the number of EBT1 and EBT3 stars decreases and the EBT2 stars show a flat distribution across the cluster, in agreement with previous results from Bedin et al. (2000) and Iannicola et al. (2009).

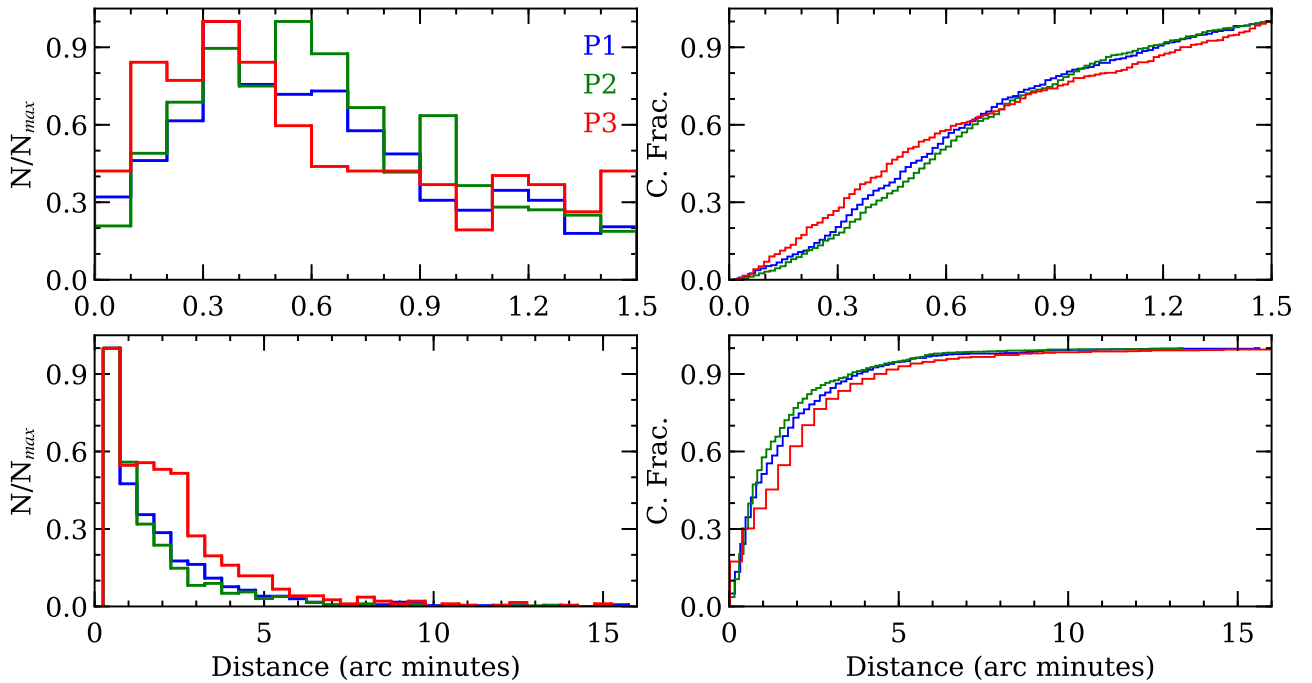


Figure 11. Top left: normalized radial distributions are shown for the P1 (blue), P2 (green), and P3 (red) populations inside $1/5$ from the cluster center. The data are binned in $0/1$ increments and are normalized relative to the most populated bin for each group. Bottom left: a similar plot using $0/5$ bins but extending out to about 70% of the tidal radius. Top right: cumulative radial distributions are shown for the three NGC 2808 populations using the same colors as the left panels. Bottom right: a similar cumulative distribution extending out to the tidal radius. These panels show that the P3 group is centrally concentrated inside about 1 half-light radius ($0/8$) and then becomes more dispersed in the outer parts of the cluster. Similarly, the P2 group is the most centrally concentrated between about 1 and 5 half-light radii.

A hypothesis to explain the decrease of EBT3 stars at larger cluster radii is that some fraction of them might originate through the “hot-flasher” scenario; in this case, the stars would be more centrally concentrated as a result of forming in a binary system or as a result of binary interactions (Moehler et al. 2004; Castellani et al. 2006). Moni Bidin et al. (2011) used GIRAFFE/VLT (ESO) spectroscopy for a sample of hot HB stars ($17,000 \text{ K} \lesssim T_{\text{eff}} \lesssim 22,000 \text{ K}$) spanning the EBT1 and EBT2 groups to monitor their radial velocities as a sign of binarity. They found no binaries among the EBT1 group but found the most probable fractions of close ($p < 10$ days) and intermediate ($p < 10\text{--}50$ days) period binaries among the EBT2 group to be 20% and 30%, respectively, thus supporting the “hot-flasher” scenario. However, we note that this study did not have any EBT3 spectra, so its connection to the warmer HB population remains to be confirmed.

Another hypothesis to explain the decrease of EBT1 and/or EBT3 stars toward the outskirts of the cluster is that a fraction of them might be the progeny of a helium-enhanced subpopulation in NGC 2808, i.e., the middle or bluest MS; these stars would then be more centrally concentrated like their MS progenitors (D’Antona & Caloi 2004; Simioni et al. 2016).

However, a clear correspondence between the different MS and RGB subpopulations and the different HB groups has not been established yet. Gratton et al. (2011) used GIRAFFE/VLT spectroscopy for a sample of 49 RHBs to show that these stars have a similar O–Na anticorrelation to the RGB stars, while the EBT1 stars are mostly Na-rich.

We matched the Gratton et al. spectroscopic data with our photometric catalog and found 37 HB stars in common and with both Na and O abundances measured. Figure 16 shows the RGB stars divided into the P1, P2, and P3 groups according to our selection and with Na and O measurement from Carretta in the $[\text{Na}/\text{Fe}]$ versus $[\text{O}/\text{Fe}]$ plane. The HB stars with Na and O

measurements from Gratton et al. are overplotted, and the figure shows that RHBs have a spread in the Na and O abundances and cover the same region spanned by the P1 and P2 RGB subpopulations and some P3 stars. On the other hand, the EBT1 stars are mostly Na-rich and overlap with the P3-enriched RGB stars and a few P2 stars on this plane. These data suggest that the RHB stars include both the primordial and the light-element-enhanced cluster subpopulations, while the EBT1 seems to be the progeny of only the more enriched RGB stars.

It is worth noting that only five EBT1 stars have spectroscopic abundances from Gratton et al., and so it is not possible to draw a firm conclusion on the EBT1-group-to-RGB correspondence. In addition, HB stars hotter than $\approx 11,500 \text{ K}$ (the so-called Grundahl u jump) have atmospheric abundances affected by radiative levitation and diffusion, and it is not possible to observe their original Na and O abundances.

From these data, it seems that RHBs are the progeny of more than one stellar subpopulation in the cluster, and possibly all three. Their radial distributions based on the DECam + HST catalog show that they are more numerous in the external regions of NGC 2808, with their number increasing by more than 30% for $r > 1/5$. The AGB stars, which should be the progeny of the RHBs, are also more prevalent in the more external regions. The RHB star spatial distribution is very similar to that of the P3 RGB subpopulation, whose stars have a more extended spatial distribution for distances larger than $1/5$. On the other hand, the blue HB stars show an opposite trend, possibly supporting a binary origin.

A similar result for the NGC 2808 RHB was found by Jain et al. (2019) using UV photometry collected with UVIT on Astrosat to study the properties of the cluster HB. Their analysis shows that the RHB is composed of at least two different subpopulations and that it has a more extended spatial distribution compared to the bluer HB stars.

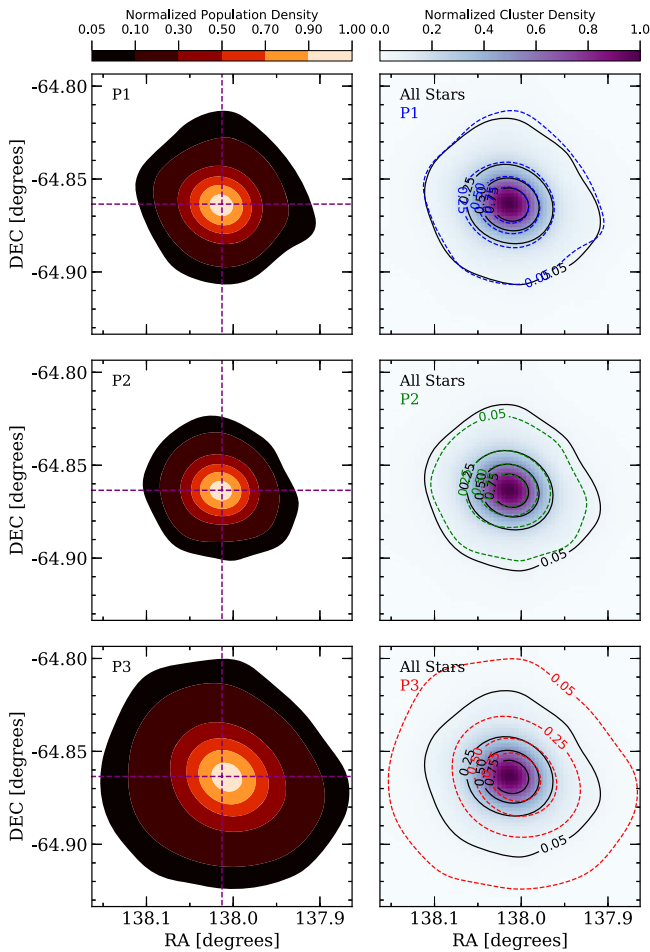


Figure 12. Left: normalized isodensity contours are shown for the P1 (top), P2 (middle), and P3 (bottom) populations. The data are normalized such that the illustrated fraction is relative to the highest-density bin for each population. The intersection of the dashed purple lines highlights the adopted cluster center. Right: the color scale map shows a similar normalized density distribution to the left panels, but using all stars in the cluster. The black contours are the same in each panel and illustrate the density distributions of the entire cluster. The blue, green, and red contours are the same relative density levels for the P1, P2, and P3 populations, respectively. The panels indicate that the P3 group is off-center from the P1 + P2 populations and also show that the P3 stars are more broadly distributed. The bottom right panel also indicates that the P3 stars may be aligned with a slightly different position angle than the rest of the cluster.

6. Discussion and Conclusions

We have demonstrated that the DECam C_{ugi} pseudocolor index, as well as its HST equivalent, is strongly correlated with an RGB star’s light-element composition, in particular the Na abundance. These data showed that NGC 2808’s RGB population can be decomposed into at least three groups and that these P1, P2, and P3 subpopulations exhibit different spatial density profiles. The P3 group, the most enriched in light elements, i.e., Na-rich, is the most centrally concentrated inside about one half-mass radius but becomes much more dispersed in the outer parts of the cluster. The P3 subpopulation centroid is also offset by $\sim 6''$ – $6''.5$ from that of the P1 and P2 groups, perhaps indicating a different origin or dynamical evolution. The P1 and P2 stars exhibit similar spatial profiles, but the more Na-enhanced P2 stars are more centrally concentrated out to about 4–5 half-mass radii.

The stronger central concentration of more Na-enhanced RGB stars found in this study is consistent with the previous

analysis by Carretta (2015), which found that the intermediate (I) and enhanced (E) RGB stars were more centrally concentrated compared to the primordial (P) stars; however, their spectroscopic sample only covered distances up to $5'$ from the cluster center. Thanks to our wide-field DECam photometric catalog, we were able, for the first time, to show that the more enhanced RGB stars, our P3 group, have a more extended spatial distribution in the outskirts of NGC 2808, almost up to its tidal radius.

Although the C_{ugi} method does not efficiently separate HB stars by their light-element compositions, the HB morphology, particularly the blue extent of the HB, is thought to be closely connected to the light-element spread of stars in a GGC (e.g., Carretta et al. 2007; Gratton et al. 2010a). Therefore, we used our deep and precise DECam + HST photometric catalog to study the spatial distribution of NGC 2808’s multimodal HB. We showed that the relative fraction of RHB stars increases at radial distances $\gtrsim 1.5$, while the blue HB stars decrease toward the outskirts of the cluster. Moreover, the R parameter, calculated as the ratio of the number of HB stars and the number of RGB stars brighter than the RHB, decreases from a value of ≈ 1.5 down to ≈ 1.0 at radial distances $\gtrsim 2'$. The ratios of the numbers of HB and RGB stars over a selected sample of MS stars showed that the culprit for the correlated decrease of the R parameter with increasing radial distance is a deficit of HB stars in the outer parts of the cluster.

The different RGB and HB radial density trends suggest that there is not a direct correspondence between an RGB star’s chemical composition and its post-RGB evolution. For example, the most Na-rich RGB stars (P3) constitute 39% of our sample at $r > 1.5$ compared to only 23% inside 1.5 from the cluster core. In contrast, the EBT1 and EBT3 stars have their highest concentrations inside 1.5 of the core, while the EBT2 population either stays the same or increases slightly outside 1.5 . On the other hand, the RHB fractional contribution increases from 40% to 53% when moving from the HST (< 1.5) to DECam (> 1.5) sample. These results are contradictory to the conventional idea of how RGB and HB stars are connected by light-element composition (i.e., that more Na-rich stars evolve to become bluer HB stars). However, we can reconcile these patterns if more than one evolutionary path exists for creating the warmest blue HB stars.

As noted in Section 5.2, Moni Bidin et al. (2011) found that at least 20%–30% of the EBT2 stars (but 0% of the EBT1 stars) in NGC 2808 are in close ($p < 10$ days) or intermediate ($p < 10$ –50 days) binary systems, and their work notes specifically that the warmer blue HB stars could result from both the binary (enhanced mass loss leading to a small HB envelope mass; the “hot-flasher” scenario) and the He enrichment (high original helium abundances pushing the low-mass stars to higher HB temperatures) channels. This scenario implies that the dual formation paths for blue HB stars at least partially erase the expected correlation between Na and He abundance and HB location.

Figure 16 shows that while the EBT1 stars correlate with the P3 RGB abundances, the RHB stars exhibit an O–Na anticorrelation that also reaches $[\text{Na}/\text{Fe}]$ values as high as $+0.4$ dex, equivalent to the $I2_{C15}$ and some E_{C15} stars from Carretta (2015; see also Figure 8) and the P3 population here. In other words, the Na-enriched P2 and P3 RGB stars can feasibly evolve to occupy almost any HB location. Furthermore, a recent analysis from Carlos et al. (2022) found at least

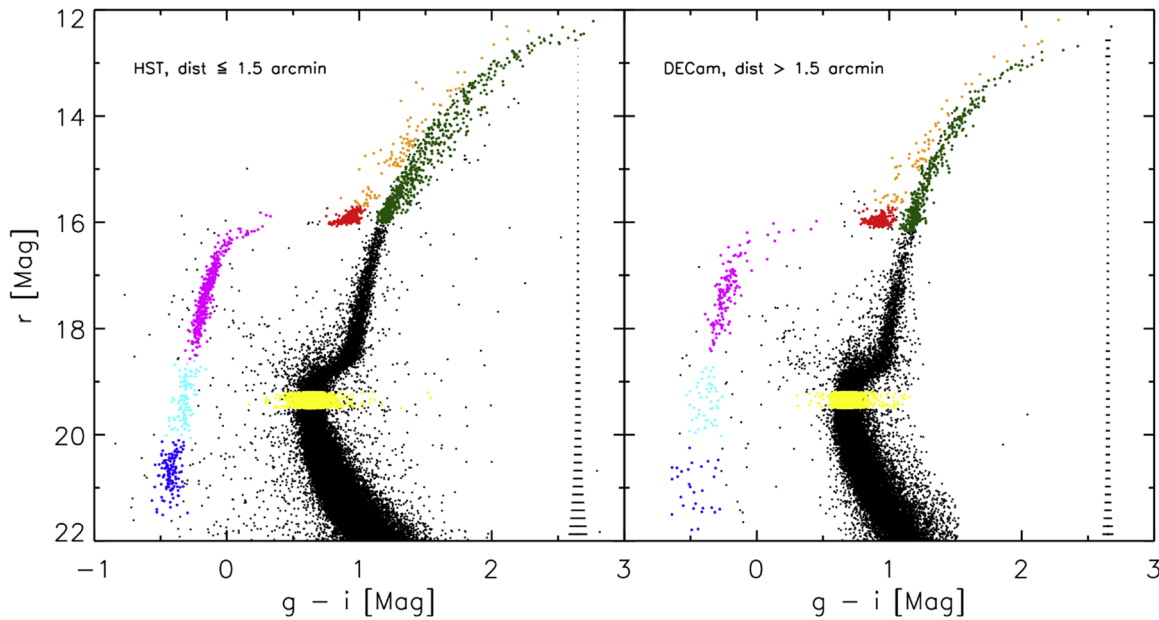


Figure 13. Left: $r, g - i$ CMD based on HST photometry for radial distances $\leq 1/5$ from the center of NGC 2808. Selected RGB, AGB, MS, and RHB stars are shown as green, orange, yellow, and red filled circles, respectively, while the blue HB stars, divided into the three groups EBT1, EBT2, and EBT3, are overlotted as magenta, cyan, and blue filled circles, respectively. Right: same as the left panel, but for distances $> 1/5$ and based on DECam photometry. Note that the HST photometry has been transformed onto the DECam photometric system (see text for more details).

one very O-poor AGB star in NGC 2808 that could not have evolved from the blue tail of the HB, as those stars have masses that are too low to ascend the AGB (e.g., see the discussion in Gratton et al. 2010b).

Further empirical evidence supporting at least some decoupling between RGB composition and HB evolution can be found when examining “second parameter clusters,” such as M3 and M13 (see also Lee et al. 1994). In this case, both clusters have similar metallicities, though possibly different ages (e.g., see discussion in Gratton et al. 2010a), along with substantial populations of primordial and enriched stars (e.g., Sneden et al. 2004; Johnson & Pilachowski 2012, see also D’Antona & Caloi 2008), but M13 contains no RHB stars and a long blue tail, while M3 exhibits a strong RHB and a much less extended blue HB. Similarly, NGC 2808 and NGC 6402 are nearly identical in metallicity, age, and mass; both clusters contain stars spanning a wide range of light-element abundances, but NGC 2808 has a very prominent RHB and long blue HB, while NGC 6402 has almost no RHB stars and a slightly truncated blue HB (Johnson et al. 2019; D’Antona et al. 2022). These two examples highlight that RGB Na and similar abundances alone cannot predict where a star will evolve to on the HB.

From the information above, we posit that our spatial density results for NGC 2808 may be explained if the RHB stars evolved from a mixture of all three RGB populations, the EBT1 stars evolved mostly from more Na- and He-enhanced (P2 and P3) single stars, and the EBT2 + EBT3 stars formed from a mixture of “hot-flasher” binaries and the most enriched P3 stars. Following D’Ercole et al. (2008) and Moni Bidin et al. (2011), the higher masses of the binary systems and initial central formation of Na- and He-enhanced stars constrain a significant fraction of these groups and their progeny near the cluster core. At larger radii, mass segregation would cause a decrease in the binary fraction that drives a decline in the EBT2 and EBT3 populations. However, if the ratio of P3 stars evolving onto the EBT2 versus EBT3 groups is high, then the

decline in the EBT2 population fraction with increasing radius would be somewhat mitigated. Similarly, dynamical interactions might be expected to drive diffusion of the more Na- and He-enhanced P2 and especially P3 stars, which could be as much as 25% ($0.2 M_{\odot}$) less massive than their “He-normal” counterparts, into the outer parts of the cluster on preferentially radial orbits (Mastrobuono-Battisti & Perets 2013; Bellini et al. 2015; Hénault-Brunet et al. 2015; Mastrobuono-Battisti & Perets 2016). This could explain the more dispersed density distribution of P3 stars outside the cluster core, and if a significant fraction of such stars can evolve onto the RHB, as well as the blue HB, then the diffusion process might explain the increasing RHB fraction with increasing radial distance as well.

These results suggest similarities between NGC 2808 and the most massive, and peculiar, GGC ω Cen. Calamida et al. (2017) and Calamida et al. (2020) used deep and precise wide-field DECam photometry, combined with HST data for the cluster center, to show that the most metal-rich RGB stars are centrally concentrated but have a more extended spatial distribution compared to the more metal-poor RGB stars; in addition, their centroid is shifted by $\approx 1'$ ($0.28 r_h$) relative to the centroid of the primordial metal-poor stellar population. Blue MS stars are also more centrally concentrated, with a more extended spatial distribution compared to the red MS.

Regarding the HB, Castellani et al. (2007) showed that the bluest HB stars in ω Cen (EBT3, or EHBs; note that ω Cen does not have an RHB) are more centrally concentrated, supporting their origin as hot flashers. This was further confirmed by the spectroscopic analyses of Moehler et al. (2007, 2011) and Latour et al. (2014), which showed that EHB stars can not only be the progeny of the supposedly helium-enhanced subpopulation in ω Censince; a large fraction of them also show C enhancement in their atmosphere, resulting from the mixing between the helium- and carbon-rich core and the hydrogen envelope (Sweigart 1997; Brown et al. 2001; Miller Bertolami et al. 2008; Cassisi et al. 2009). On the other hand, a radial

Table 4

The Number of HB Stars in the Four HB Groups on the RGB and on the MS Selected Area from the HST and DECam $r, g - i$ CMDs (Figure 13) Detected in the Two Different Spatial Regions of NGC 2808

Radius	$N(\text{RHB})$	$N(\text{EBT1})$	$N(\text{EBT2})$	$N(\text{EBT3})$	$N(\text{HB})$	$N(\text{RGB})$	$N(\text{AGB})$	$N(\text{MS})$	R
$r \leq 1.5^{\text{a}}$	484 (40% \pm 2%)	416 (35% \pm 2%)	112 (11% \pm 1%)	132 (14% \pm 1%)	1144 ± 34	761 ± 26	102 ± 10	6725 ± 82	1.50 ± 0.03
$r > 1.5^{\text{b}}$	274 (53% \pm 4%)	139 (25% \pm 3%)	48 (13% \pm 2%)	29 (9% \pm 1%)	490 ± 22	437 ± 21	71 ± 8	3405 ± 58	1.16 ± 0.27
Total	758 ± 27	555 ± 23	160 ± 13	161 ± 13	1634 ± 40	1198 ± 35	173 ± 13	10130 ± 101	...

Notes. Values within parentheses give for each region the relative fraction of the different groups with respect to the total number of HB stars. The R parameter values are also listed.

^a Star counts based on HST data.

^b Star counts based on DECam data.

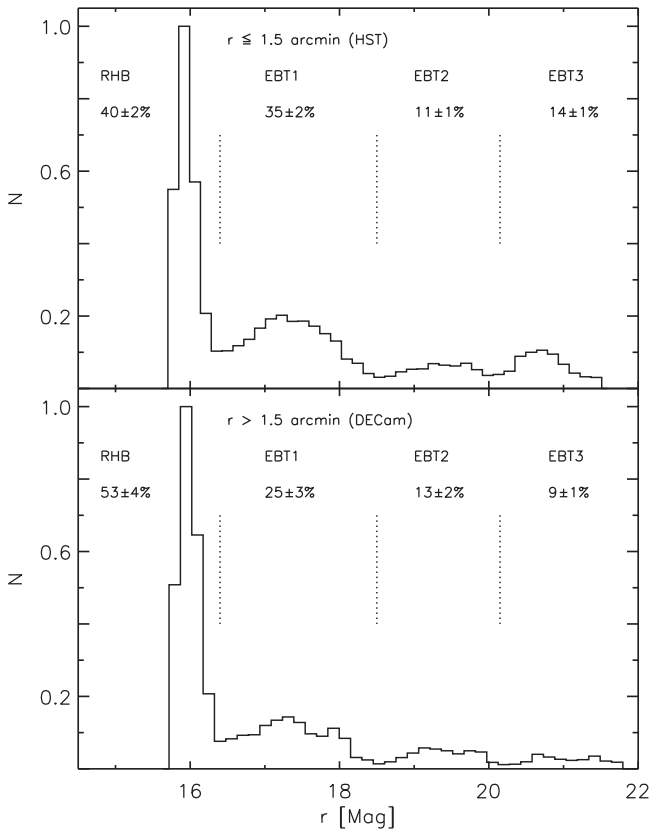


Figure 14. Top: r -band luminosity distribution of the different HB groups in NGC 2808, RHB, EBT1, EBT2, and EBT3, respectively, for radial distances from the cluster center ≤ 1.5 and based on HST photometry. Bottom: same as the top panel, but for distances > 1.5 and based on DECam photometry.

velocity study of 152 EHB stars in ω Cen showed a close-binary fraction of only $\approx 5\%$ (Latour et al. 2018). However, this analysis was not sensitive to intermediate- and long-period binaries, which could be the majority of the EHB binaries, such as Moni Bidin et al. (2011) have shown in NGC 2808.

The analyses presented here and in Calamida et al. (2017, 2020) highlight the power of extending population investigations beyond a few half-light radii with wide-field imagers, especially for massive GGCs. Radial density trends observed in small HST fields are not necessarily representative of a cluster's global properties, and we do not yet have a clear enough understanding about post-RGB evolution to fully link the different groups identified in MS, RGB, HB, and AGB

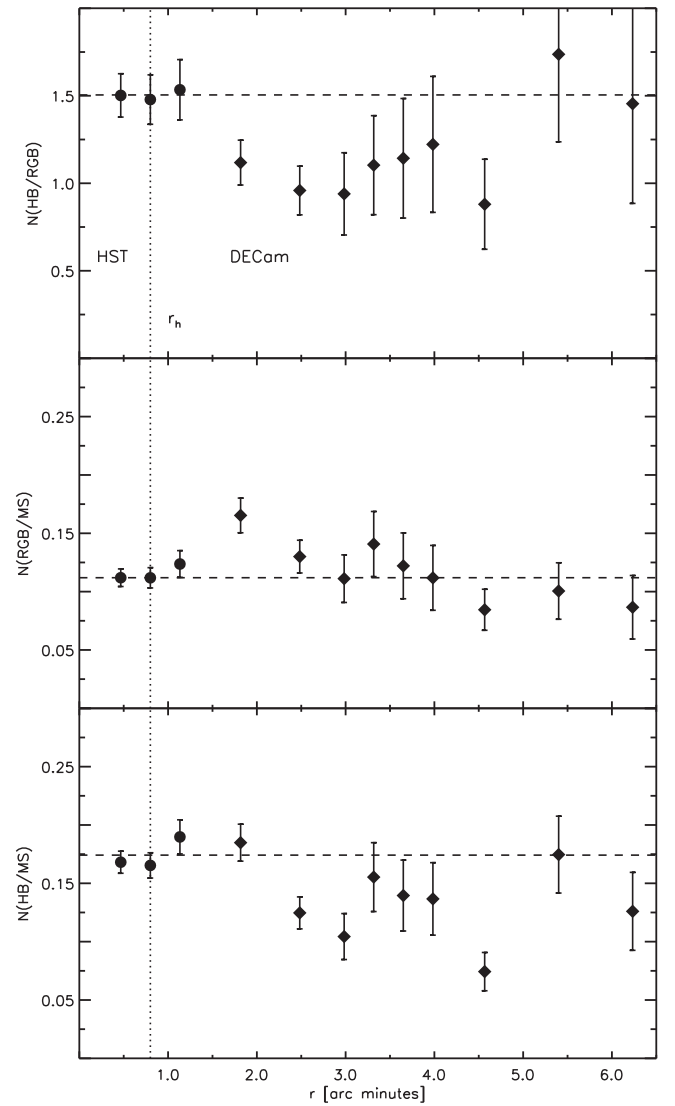


Figure 15. Top: R parameter plotted as a function of distance from the cluster center and based on HST and DECam star counts. Middle: same as the top panel, but for the ratio of the number of RGB and MS stars. Bottom: same as the top panel, but for the ratio of the number of HB and MS stars.

analyses. However, renewed investigations into the outer parts of clusters, where dynamical evolution times are longer, with space-based UV imaging, ground-based wide-field imaging (e.g., DECam C_{ugi}), and spectroscopic abundance analyses and radial velocity monitoring should provide new insight into the

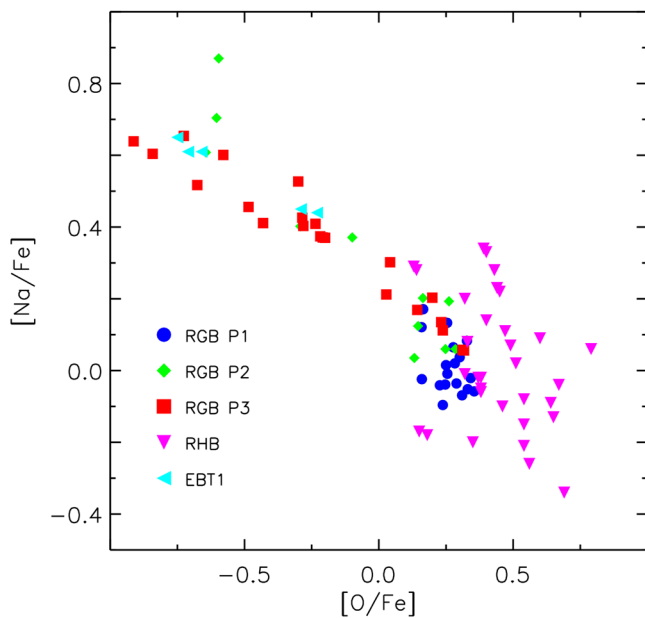


Figure 16. $[\text{Na}/\text{Fe}]$ vs. $[\text{O}/\text{Fe}]$ abundance for RGB stars in common with the spectroscopic study of Carretta (2015) divided into our identified three subpopulation groups, P1 ($N_s = 21$; blue filled circles), P2 ($N_s = 13$; green diamonds), and P3 ($N_s = 25$; red squares). HB stars in common with the study of Gratton et al. (2011) are also overplotted and divided into RHBs ($N_s = 32$; magenta downward-pointing triangles) and EBT1 stars ($N_s = 5$; cyan leftward-pointing triangles).

complicated formation histories of the galaxy’s globular clusters.

C.A.P. acknowledges the generosity of the Kirkwood Research Fund at Indiana University. A.M.-B. acknowledges funding from the European Union’s Horizon 2020 research and innovation program under the Marie Skłodowska-Curie grant agreement No. 895174. This study was supported by the DDRF grant D0001.82481. This project used data obtained with the Dark Energy Camera (DECam), which was constructed by the Dark Energy Survey (DES) collaboration. Funding for the DES Projects has been provided by the U.S. Department of Energy, the U.S. National Science Foundation, the Ministry of Science and Education of Spain, the Science and Technology Facilities Council of the United Kingdom, the Higher Education Funding Council for England, the National Center for Supercomputing Applications at the University of Illinois at Urbana-Champaign, the Kavli Institute of Cosmological Physics at the University of Chicago, the Center for Cosmology and Astro-Particle Physics at The Ohio State University, the Mitchell Institute for Fundamental Physics and Astronomy at Texas A&M University, Financiadora de Estudos e Projetos, Fundação Carlos Chagas Filho de Amparo à Pesquisa do Estado do Rio de Janeiro, Conselho Nacional de Desenvolvimento Científico e Tecnológico and the Ministério da Ciência, Tecnologia e Inovação, the Deutsche Forschungsgemeinschaft, and the Collaborating Institutions in the Dark Energy Survey. The Collaborating Institutions are Argonne National Laboratory, the University of California at Santa Cruz, the University of Cambridge, Centro de Investigaciones Energéticas, Medioambientales y Tecnológicas-Madrid, the University of Chicago, University College London, the DES-Brazil Consortium, the University of Edinburgh, the Eidgenössische Technische Hochschule (ETH) Zürich, Fermi National Accelerator

Laboratory, the University of Illinois at Urbana-Champaign, the Institut de Ciències de l’Espai (IEEC/CSIC), the Institut de Física d’Altes Energies, Lawrence Berkeley National Laboratory, the Ludwig-Maximilians Universität München and the associated Excellence Cluster Universe, the University of Michigan, the National Optical Astronomy Observatory, the University of Nottingham, The Ohio State University, the OzDES Membership Consortium the University of Pennsylvania, the University of Portsmouth, SLAC National Accelerator Laboratory, Stanford University, the University of Sussex, and Texas A&M University. Based on observations at Cerro Tololo Inter-American Observatory, National Optical Astronomy Observatory, which is operated by the Association of Universities for Research in Astronomy (AURA) under a cooperative agreement with the National Science Foundation. This work has made use of data from the European Space Agency (ESA) mission Gaia (<https://www.cosmos.esa.int/gaia>), processed by the Gaia Data Processing and Analysis Consortium (DPAC; <https://www.cosmos.esa.int/web/gaia/dpac/consortium>). Funding for the DPAC has been provided by national institutions, in particular the institutions participating in the Gaia Multilateral Agreement.

Facilities: CTIO:4.0 m, HST:WFC3, HST:ACS.

ORCID iDs

Christian I. Johnson <https://orcid.org/0000-0002-8878-3315>

Annalisa Calamida <https://orcid.org/0000-0002-0882-7702>

Justin A. Kader <https://orcid.org/0000-0002-6650-3757>

Catherine A. Pilachowski <https://orcid.org/0000-0002-3007-206X>

Giuseppe Bono <https://orcid.org/0000-0002-4896-8841>

Alessandra Mastrobuono-Battisti <https://orcid.org/0000-0002-2386-9142>

Armin Rest <https://orcid.org/0000-0002-4410-5387>

Alfredo Zenteno <https://orcid.org/0000-0001-6455-9135>

Alice Zocchi <https://orcid.org/0000-0001-8075-3149>

References

- Bastian, N., Lamers, H. J. G. L. M., de Mink, S. E., et al. 2013, *MNRAS*, **436**, 2398
- Bedin, L. R., Piotto, G., Zoccali, M., et al. 2000, *A&A*, **363**, 159
- Bellini, A., Vesperini, E., Piotto, G., et al. 2015, *ApJL*, **810**, L13
- Brown, T. M., Sweigart, A. V., Lanz, T., Landsman, W. B., & Hubeny, I. 2001, *ApJ*, **562**, 368
- Calamida, A., Strampelli, G., Rest, A., et al. 2017, *AJ*, **153**, 175
- Calamida, A., Zocchi, A., Bono, G., et al. 2020, *ApJ*, **891**, 167
- Cardelli, J. A., Clayton, G. C., & Mathis, J. S. 1989, *ApJ*, **345**, 245
- Carlos, M., Marino, A. F., Milone, A. P., et al. 2022, *MNRAS*, **519**, 1695
- Carretta, E. 2015, *ApJ*, **810**, 148
- Carretta, E., Bragaglia, A., Gratton, R. G., et al. 2009, *A&A*, **505**, 117
- Carretta, E., Recio-Blanco, A., Gratton, R. G., Piotto, G., & Bragaglia, A. 2007, *ApJL*, **671**, L125
- Cassisi, S., Salaris, M., Anderson, J., et al. 2009, *ApJ*, **702**, 1530
- Cassisi, S., Salaris, M., & Irwin, A. W. 2003, *ApJ*, **588**, 862
- Castellani, V., Calamida, A., Bono, G., et al. 2007, *ApJ*, **663**, 1021
- Castellani, V., Iannicola, G., Bono, G., et al. 2006, *A&A*, **446**, 569
- Catelan, M., Borissova, J., Sweigart, A. V., & Spassova, N. 1998, *ApJ*, **494**, 265
- D’Antona, F., Bellazzini, M., Caloi, V., et al. 2005, *ApJ*, **631**, 868
- D’Antona, F., & Caloi, V. 2004, *ApJ*, **611**, 871
- D’Antona, F., & Caloi, V. 2008, *MNRAS*, **390**, 693
- D’Antona, F., Milone, A. P., Johnson, C. I., et al. 2022, *ApJ*, **925**, 192
- D’Antona, F., Vesperini, E., D’Ercole, A., et al. 2016, *MNRAS*, **458**, 2122
- D’Cruz, N. L., Dorman, B., Rood, R. T., & O’Connell, R. W. 1996, *ApJ*, **466**, 359

- D'Ercole, A., Vesperini, E., D'Antona, F., McMillan, S. L. W., & Recchi, S. 2008, *MNRAS*, **391**, 825
- de Boer, T. J. L., Gieles, M., Balbinot, E., et al. 2019, *MNRAS*, **485**, 4906
- Gaia Collaboration 2022, VizieR On-line Data Catalog: [I/355](#)
- Gaia Collaboration, Helmi, A., van Leeuwen, F., et al. 2018, *A&A*, **616**, A12
- Gratton, R. G., Carretta, E., Bragaglia, A., Lucatello, S., & D'Orazi, V. 2010a, *A&A*, **517**, A81
- Gratton, R. G., D'Orazi, V., Bragaglia, A., Carretta, E., & Lucatello, S. 2010b, *A&A*, **522**, A77
- Gratton, R. G., Lucatello, S., Carretta, E., et al. 2011, *A&A*, **534**, A123
- Harris, W. E. 2010, arXiv:[1012.3224](#)
- Hénault-Brunet, V., Gieles, M., Agertz, O., & Read, J. I. 2015, *MNRAS*, **450**, 1164
- Hong, S., Lim, D., Chung, C., et al. 2021, *AJ*, **162**, 130
- Iannicola, G., Monelli, M., Bono, G., et al. 2009, *ApJL*, **696**, L120
- Jain, R., Vig, S., & Ghosh, S. K. 2019, *MNRAS*, **485**, 2877
- Johnson, C. I., Caldwell, N., Michael Rich, R., Mateo, M., & Bailey, J. I. 2019, *MNRAS*, **485**, 4311
- Johnson, C. I., & Pilachowski, C. A. 2012, *ApJL*, **754**, L38
- Johnson, C. I., Rich, R. M., Young, M. D., et al. 2020, *MNRAS*, **499**, 2357
- Lardo, C., Bellazzini, M., Pancino, E., et al. 2011, *A&A*, **525**, A114
- Latour, M., Husser, T. O., Giesers, B., et al. 2019, *A&A*, **631**, A14
- Latour, M., Randall, S. K., Calamida, A., Geier, S., & Moehler, S. 2018, *A&A*, **618**, A15
- Latour, M., Randall, S. K., Fontaine, G., et al. 2014, *ApJ*, **795**, 106
- Lee, Y.-W., Demarque, P., & Zinn, R. 1994, *ApJ*, **423**, 248
- Lee, Y.-W., Joo, S.-J., Han, S.-I., et al. 2005, *ApJL*, **621**, L57
- Mastrobuono-Battisti, A., & Perets, H. B. 2013, *ApJ*, **779**, 85
- Mastrobuono-Battisti, A., & Perets, H. B. 2016, *ApJ*, **823**, 61
- McLaughlin, D. E., & van der Marel, R. P. 2005, *ApJS*, **161**, 304
- Miller Bertolami, M. M., Althaus, L. G., Unglaub, K., & Weiss, A. 2008, *A&A*, **491**, 253
- Milone, A. P., Marino, A. F., Cassisi, S., et al. 2012, *ApJL*, **754**, L34
- Milone, A. P., Marino, A. F., Piotto, G., et al. 2015a, *ApJ*, **808**, 51
- Milone, A. P., Marino, A. F., Piotto, G., et al. 2015b, *MNRAS*, **447**, 927
- Milone, A. P., Piotto, G., Renzini, A., et al. 2017, *MNRAS*, **464**, 3636
- Moehler, S., Dreizler, S., Lanz, T., et al. 2007, *A&A*, **475**, L5
- Moehler, S., Dreizler, S., Lanz, T., et al. 2011, *A&A*, **526**, A136
- Moehler, S., Sweigart, A. V., Landsman, W. B., Hammer, N. J., & Dreizler, S. 2004, *A&A*, **415**, 313
- Monelli, M., Milone, A. P., Stetson, P. B., et al. 2013, *MNRAS*, **431**, 2126
- Moni Bidin, C., Villanova, S., Piotto, G., & Momany, Y. 2011, *A&A*, **528**, A127
- Nardiello, D., Libralato, M., Piotto, G., et al. 2018, *MNRAS*, **481**, 3382
- Pietrinferni, A., Hidalgo, S., Cassisi, S., et al. 2021, *ApJ*, **908**, 102
- Piotto, G., Bedin, L. R., Anderson, J., et al. 2007, *ApJL*, **661**, L53
- Piotto, G., Milone, A. P., Bedin, L. R., et al. 2015, *AJ*, **149**, 91
- Sandquist, E. L., & Martel, A. R. 2007, *ApJL*, **654**, L65
- Sarajedini, A., Bedin, L. R., Chaboyer, B., et al. 2007, *AJ*, **133**, 1658
- Schlafly, E. F., & Finkbeiner, D. P. 2011, *ApJ*, **737**, 103
- Simioni, M., Milone, A. P., Bedin, L. R., et al. 2016, *MNRAS*, **463**, 449
- Snedden, C., Kraft, R. P., Guhathakurta, P., Peterson, R. C., & Fulbright, J. P. 2004, *AJ*, **127**, 2162
- Sohn, Y.-J., Byun, Y.-I., Yim, H.-S., Rhee, M.-H., & Chun, M.-S. 1998, *JASS*, **15**, 1
- Sosin, C., Dorman, B., Djorgovski, S. G., et al. 1997, *ApJL*, **480**, L35
- Stetson, P. B. 1987, *PASP*, **99**, 191
- Stetson, P. B. 1990, *PASP*, **102**, 932
- Sweigart, A. V. 1997, *ApJL*, **474**, L23
- Sweigart, A. V., & Catelan, M. 1998, *ApJL*, **501**, L63
- Tiongco, M. A., Vesperini, E., & Varri, A. L. 2022, *MNRAS*, **512**, 1584
- Trager, S. C., King, I. R., & Djorgovski, S. 1995, *AJ*, **109**, 218
- Valdes, F., & Gruendl, R. 2014, in ASP Conf. Ser. 485, *Astronomical Data Analysis Software and Systems XXIII*, ed. N. Manset & P. Forshay (San Francisco, CA: ASP), 379
- Valle, G., Dell'Omodarme, M., & Tognelli, E. 2022, *A&A*, **658**, A141
- Vasiliev, E., & Baumgardt, H. 2021, *MNRAS*, **505**, 5978
- Vesperini, E., Hong, J., Giersz, M., & Hypki, A. 2021, *MNRAS*, **502**, 4290
- Vesperini, E., McMillan, S. L. W., D'Antona, F., & D'Ercole, A. 2013, *MNRAS*, **429**, 1913
- Walker, A. R. 1999, *AJ*, **118**, 432
- Zoccali, M., Cassisi, S., Bono, G., et al. 2000, *ApJ*, **538**, 289